Department of Precision and Microsystems Engineering

Metamaterial Behaviour for Motion Systems Using an Approximated Ideal Shear Cell

L. H. Schattenberg

Report no : 2024.090
Coach : PhD. P. Roberjot
Professor : Dr. Ir. J. L. Herder
Specialisation : High-Tech Engineering
Type of report : MSc Thesis
Date : 12 October 2024

Abstract

Metamaterials are tessellated structures that introduce unique properties to motion system applications. The research on behaviour changes caused by this tessellation remains limited. This paper outlines the change in behaviour from a compliant unit cell to a metamaterial motion system, regarding linear stiffness, range of motion (RoM) and crosstalk. These properties are achieved through the analysis of series and parallel configurations, as well as scaling variations. The concept of an ideal shear cell is presented, describing desired motion system characteristics. Roberts mechanism approximates the ideal shear cell, bringing embodiment for finite element analysis and experimental validation. Results indicate that parallel configurations increase stiffness, while series arrangements reduce it, with RoM and crosstalk displaying opposing trends. Additionally, variations in flexure thickness introduce a trade-off between stiffness and range of motion. Different scaling strategies affect overall stiffness with minimal impact on RoM and crosstalk. While the main findings do not indicate inherent performance benefits to compliant mechanisms. This research contributes valuable insights into the design and performance of metamaterial-based motion systems, providing a foundational framework for future studies and applications.

Contents

1 Introduction

Metamaterials are engineered structures, exhibiting special properties uncommon or not found in nature[1][2]. These include features such as negative or zero Poisson's ratio[3][4][1], tunable stiffness[5], multistability[6][7] and shape memory[8]. Their specialized design arises from carefully structured unit cells that can be tailored to achieve particular mechanical responses. Motion systems, on the other hand, typically comprise three fundamental components: a guiding structure, an actuator and a sensor[9]. Combining these fields can result in more compact motion systems by incorporating the actuation and sensing into the guiding structure. Additionally, distributed actuation introduces new behaviour as active tuning of stiffness[10] and damping. Next to the properties induced from internal actuation, the traditional metamaterial properties can add numerous functionalities.

Research on the impact of tessellating unit cells on metamaterial behaviour remains limited. Multistability provides a compelling example of the number serial unit cells increasing the amount of stable positions[6][7], however as most metamaterials the analysis includes a single property. Zhang et al. [11] provided more elaborate analysis, including the investigation of the tilted stable configurations depending on the amount of parallel unit cells. Another research direction is metamaterial mechanisms[12], where unit cells are systematically arranged to replicate the functions of traditional mechanical components. Another topic of research is configuration indifferent building blocks [13], where the relative positions of the unit cells do not affect the overall degrees of freedom. Each of these approaches represents a step forward in leveraging metamaterial structures to enhance and expand the capabilities of motion-based applications. However, a general study on motion properties is still missing. Additionally, guidelines for determining the number and scale of unit cells is not yet present.

This paper answers the question: how do stiffness, range of motion and crosstalk change from a compliant mechanism to a low number metamaterial motion system? The metamaterial behaviour is split into two topics, the number of unit cells denoted as m x n and the size of these unit cells. A unit cell is designed using the concept of an ideal shear cell, which builds upon the research of metamaterial mechanisms[12]. With a unit cell selected, in plane tessellation and scaling are analysed with an analytical model, finite element simulations and experimental validation. The results outline the effect of the number of serial and parallel unit cells, and their overall size. Guidelines are formed for metamaterial motion system design. This enables future research directions, including internal sensor and actuator placement for distributed mechatronics and more complex 3 dimensional metamaterial tessellations.

Subsection 2.1 starts by introducing the concept of an ideal shear cell, including examples to approximate its behaviour. A unit cell is selected, adapted and analysed in subsubsection 2.2.1. The main analysis starts in subsection 2.3, where the analytical model for the series, parallel and scaling variations are derived. The setups for FEM and experiment are explained in subsection 2.4 and subsection 2.5. Following the analysis, the results are presented in section 3. The results are discussed in section 4, followed by a conclusion in section 5.

2 Methods

This section begins by introducing the ideal shear cell in subsection 2.1. In subsubsection 2.2.1 a unit cell is selected and adapted for metamaterial tessellation. The properties of interest are calculated, after which the main analysis begins. The variations of parallel, series and scaling are modelled analytically in subsection 2.3, followed by the finite element and experimental setups in sections subsection 2.4 and subsection 2.5.

2.1 Ideal shear cell

Ion et al. [12] propose the concept of metamaterial mechanisms, using building blocks to generate a mechanism. One of the building blocks is the shear cell, as shown in Figure 1. The shear cell is a square consisting of stiff edges and flexible corners, allowing rotation of the edges. The shearing motion follows a circular trajectory as shown in Figure 1b, meaning significant crosstalk between the shearing motion and the downward displacement. At the extreme position, this downwards displacement is equal to the horizontal displacement. The shear cell is improved by eliminating the crosstalk, leading to the concept of an ideal shear cell as shown in Figure 1c. For applications in motion systems this concept generates linear motion, while constraining the remaining degrees of freedom. In addition to describing the behaviour in motion terms, it can similarly be explained using stiffness. In an ideal motion system the degree of freedom (DoF) exhibits zero stiffness, while the constraints are infinitely stiff. More specifically the shear motion exhibits zero stiffness, while the remaining two translations and the three orthogonal rotations are infinitely stiff.

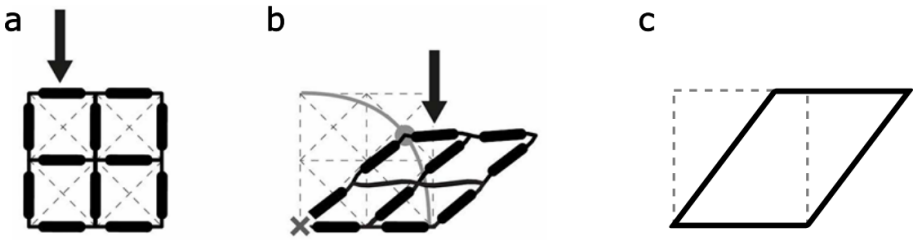

Figure 1: (a) Shear cell proposed by Ion et al. [12], undeformed state. (b) Deformed state showing the circular trajectory of the top left corner in grey. (c) Abstract boundary of the ideal shear cell, shear motion without vertical displacement

A double leaf spring, shown in Figure 2a, matches the shear cell of Ion et al. [12] in Pseudo Rigid-Body Model (PRBM). A common improvement of the double leaf spring is a folded flexure linear guide, shown in Figure 2b. The crosstalk is compensated by placing a second flexure mechanism on the original output link, functioning as an intermediate body. Each flexure has a decrease in height, therefore the intermediate body has crosstalk but the new output link is compensated by the equal decrease of flexure length between the coupler body and the output. Apart from this common design, three different design approaches are presented.

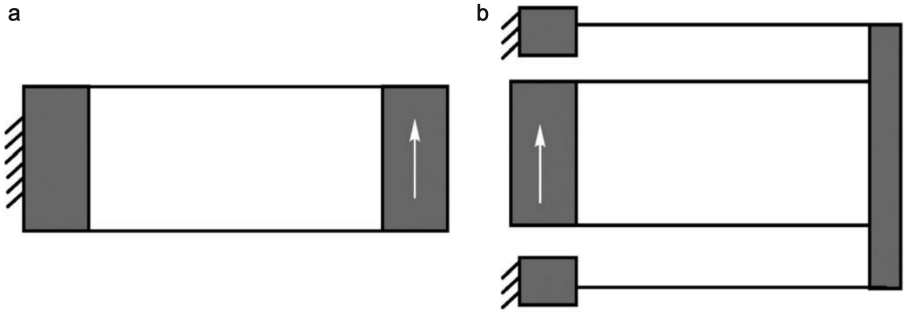

Figure 2: [14](a) Double leaf spring and (b) folded flexure linear guide

The first design approach is compliant rolling-contact architected materials (CRAMs)[15]. CRAMs use flexures to constrain rolling contact between rigid bodies. Figure 3 shows three states of a rack and pinion mechanism, produced with CRAMs. The first state is unassembled, where the rigid bodies and flexures are clearly visible. To form the CRAM, the flexures are alternated in sequence and deformed until the different layers of cams are joined together. This configuration constrains the cams to maintain rolling contact with

the racks. Lastly, the deformed state shows the motion comparable to the ideal shear cell. Predeforming the flexures results in a constant energy during motion, allowing zero stiffness for an optimised design. Coupled with high constraint stiffness this results in large ratio's between the DoF and the constraints. Furthermore, the rolling contact, ensures pure shear motion if the cams are perfect circular cylinders. However, the downside of CRAMs is that the mechanisms require assembly. This effect can be replicated at micro scale but requires specialised procedures and equipment[15].

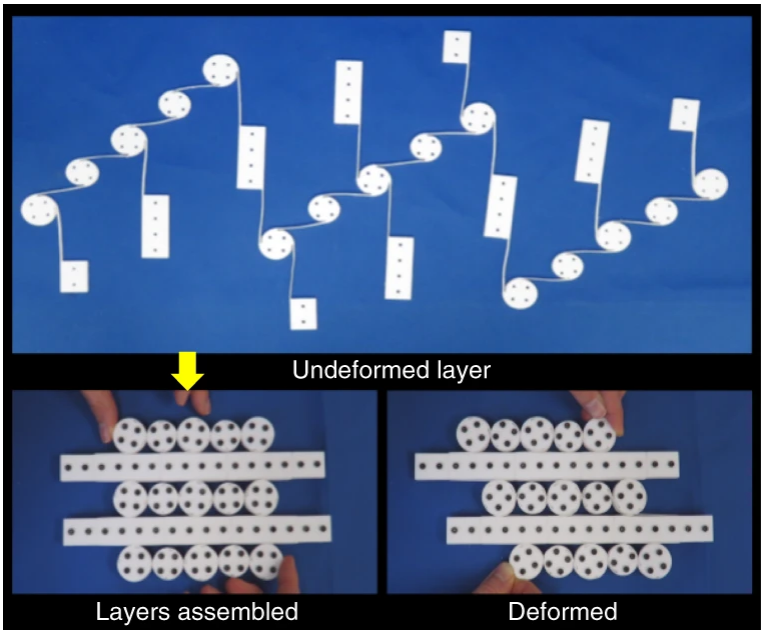

Figure 3: Compliant rolling-contact architected materials[15]

The second design approach is the family of straight-line mechanisms. Straight-line mechanisms generate approximate or exact straight-line motion[16], at a single point or a complete body. In literature many mechanisms are found, Riutort [16] for instance analysed four-bar approximate straight-line mechanisms based on their range of motion (RoM) and encapsulated area. Included in the analysis were Watt, Hoeken, Evans, Evans-de Jonge, Chebbyschev and Roberts mechanisms. From the analysed mechanisms, Roberts type 1 is the most compact, shown in Figure 4a. Roberts mechanism is an approximate straight-line mechanism for a single point P. Coupling two such mechanisms will extend the straight-line motion from a single point to a coupling link, going from path generation to motion generation[17] or to linear-motion mechanism[18]. Figure 4b shows a compliant version of Roberts mechanism, using this coupling technique with link P_1P_2.

Exact straight-line mechanisms can include in plane mechanisms including Peaucellier-Lipkin[19][20] or more 3 dimensional mechanisms such as Sarrus mechanism[21][22]. The primary advantage of straight-line mechanisms is that there are numerous mechanisms documented in literature, part of which are already compliant. A potential downside is that some mechanisms, such as Peaucellier-Lipkin, are more complex and their compliant counterparts[19] have limited RoM.

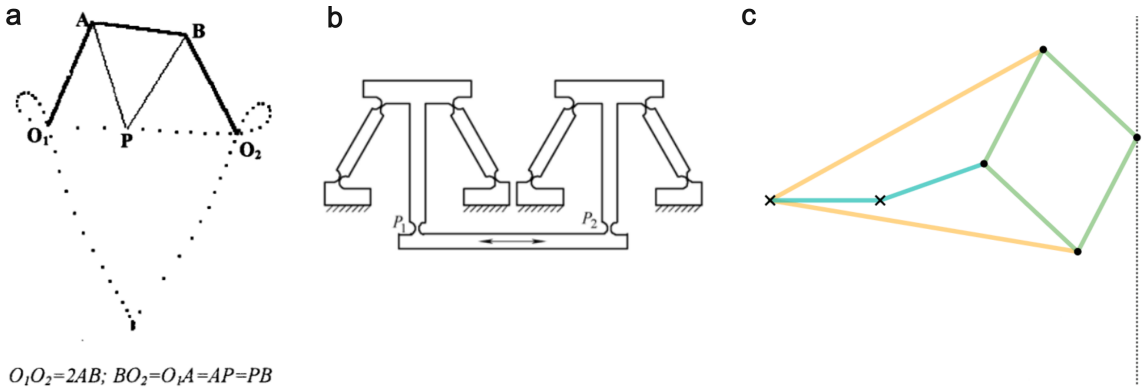

Figure 4: (a) Roberts linkage and its corresponding trajectory[16], (b) compliant Roberts linkage with linear-motion of link P_1P_2[18] and (c) exact straight-line mechanism Peaucellier-Lipkin[20]

Lastly the design approach of error compensation. Zhao, Bi, and Yu [23] use generalised cross-spring pivots to analyse and eliminate parasitic motion of four bar mechanisms. The cross-spring pivot may consist of a cross flexure, however the intersection of the leaf springs does not have coincide within the flexure, as shown in Figure 5 a and b. Figure 5a shows the working principle, the center shift of the cross flexures increases the distance between the joints[24]. When dimensioned correctly, this method fully compensates for the parasitic motion in a four-bar mechanism. Figure 5b shows this method using two generalised cross-spring pivots to design a different building block, similar the Xbob[25]. The method is used to generate families of designs, one of which is shown in Figure 5c. The advantage of this approach is the elimination of parasitic motion, similar to exact straight-line mechanisms.

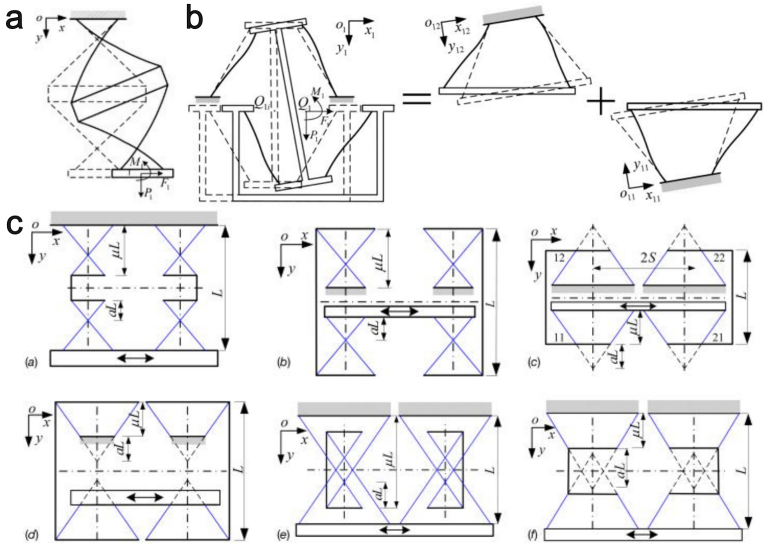

Figure 5: Error compensation. (a) Working principle generalised cross pivots[23] (b) Double Roberts mechanism using generalised cross pivots[24], also named XBob[25] (c) Family of designs using this technique, flexures shown in blue and rigid frames in black.[24]

The three presented design approaches offer various methods to approximate an ideal shear cell for motion system applications. Based on these concepts, the next section will select and adapt a unit cell for tessellation.

2.2 Unit cell

In this section the unit cell is chosen and adapted for metamaterial tessellation. The different parameters of interest are presented and modelled analytically. An initial FEM analysis is carried out to verify intermediate results.

2.2.1 Unit cell design

To select a unit cell, the method of weighted criteria is used. First criteria are sorted in order, after which weights are assigned. Each concept is graded, after which the grades are multiplied by the weights and summed. The highest scoring design is chosen for further analysis.

For this research, the unit cell is designed after which extensive modelling, simulations and experiments are carried out. Therefore, the unit cell should be simple and easy to fabricate. For this analysis, the performance, how well the unit cell approximates the ideal shear cell, is less important as this design is not optimised for application. If a design is required for practical use, then the performance criteria are more important than the manufacturing and design criteria. Table 1 shows the ordered criteria and the assigned weights 1 to 5.

Table 1: Criteria and their weights

Criteria	Weight
Readiness	5
Manufacturability	4
Compact	3
Stiffness ratio	2
Crosstalk	1

Each design is qualitatively graded with 1 performing poor, 2 performing average and 3 performing well. This method is chosen as many designs do not specify the full range of criteria. In the list below, the criteria are explained and grades are determined.

- Readiness: How much modification the design requires, preferably without extensive derivations for the unit cell itself. This allows the research to focus on the relative behaviour.
- Manufacturability: How complex the geometry is and how much assembly is required. As many samples are required for analysis, the manufacturing should be fast and cheap. Complex 3D geometries either require more advanced production techniques or assembly.
- Compact: A compact design has a high RoM compared to the design area.
- Stiffness: The stiffness ratio is a measure of how well the motion system behaves. A low DoF stiffness and a high DoC stiffness are desired.
- Crosstalk: The coupling between desired and undesired motion.

Table 2: Design concepts graded using weighted criteria

Criteria	Weight	Robert		Peaucellier		CRAM		Error comp		FoldedFlex		Doubleleaf	
Readiness	5	3	15	1	5	2	10	1	5	3	15	3	15
Manufacturability	4	3	12	3	12	1	4	2	8	3	12	3	12
Compact	3	3	9	2	6	3	9	2	6	2	6	2	6
Stiffness	2	2	4	2	4	3	6	2	4	2	4	2	4
Crostalk	1	2	2	3	3	3	3	3	3	3	3	1	1
Total		42		30		32		26		34		38	

- Roberts mechanism: A 2.5 D design, which is easy to fabricate (manufacturability 3). There are numerous examples in literature, requiring minor modifications (readiness 3). The mechanism is one of the most compact straight line mechanisms (compact 3). The mechanism has crosstalk and approximates a straight line (crosstalk 2). Lastly the compliant version requires force to move while having moderate constraint stiffness (stiffness 2)

- Peaucellier - Lipkin mechanism: The mechanism requires a major redesign to obtain a large RoM compliant version (readiness 1). The mechanism is 2.5 D, as no links or joints overlap (manufacturability 3). The mechanism has a slightly larger footprint compared to Roberts mechanism (compact 2). The stiffness is expected to be moderate, as the configuration loads the joints on bending and torsion, while also requiring force to deflect (stiffness 2). The mechanism is an exact straight line mechanism (crosstalk 3).

- CRAM: Cram requires more complex analysis to compute the stiffnesses, however there is a good example design to work from (readiness 2). The mechanism requires extensive assembly, forming the sheets into multiple layers (manufacturability 1). CRAM is compact as the displacement is bound to the perimeter of the cams (compact 3). The stiffness ratio is high, as near zero actuation force is required and the constraints are stiff (stiffness 3). The crosstalk is low, only depending on the tolerance of the cylinders (crosstalk 3)

- Folded flexure: The folded flexure is well established, requiring minor changes and is straightforward to analyse (readiness 3). The mechanism is 2.5 D and can be monolithically produced (manufacturability 3). The mechanism is limited by stress and typically requires a large design area (compact 2). The stiffness is similar to the other compliant mechanisms, requiring increasing actuation force and and having moderate stiffness (stiffness 2). The crosstalk is compensated by the second stage of flexures (crosstalk 3).

- Double leaf spring: Only two parallel leaf springs and well known behaviour (readiness 3). 2.5 D design (manufacturability 3). The RoM is limited[14] (compact 2). The stiffness ratio is expected to be comparable to the folded flexure and Roberts mechanism (stiffness 2). Similar motion to the original shear cell, following an arc (crosstalk 1).

The highest score is obtained by Roberts mechanism, as it is a well known design that also performs well for motion application. If manufacturing and readiness are less important than the motion performance, the CRAM approach best approximates the ideal shear cell. For this project the assembly and more elaborate design, would leave limited time for the desired analysis.

For the unit cell design, a compliant version of Roberts mechanism is used. For large RoM, leaf springs are used on links O_1A and $O2B$ of Figure 4a[26][18]. To allow straightforward tessellation a C-shaped frame is placed around the mechanism. This ensures that the input link is at the opposite side of the base link. The reference design uses a small length flexure, capable of small rotations. For larger displacements this joint is replaced by a cartwheel[27], as it is 2.5 D geometry that allows for larger rotation. The adapted unit cell is illustrated in Figure 6, showing two unit cells in parallel. Figure 7 shows an isometric sketch of the unit cell, setting the convention for x, y and z directions.

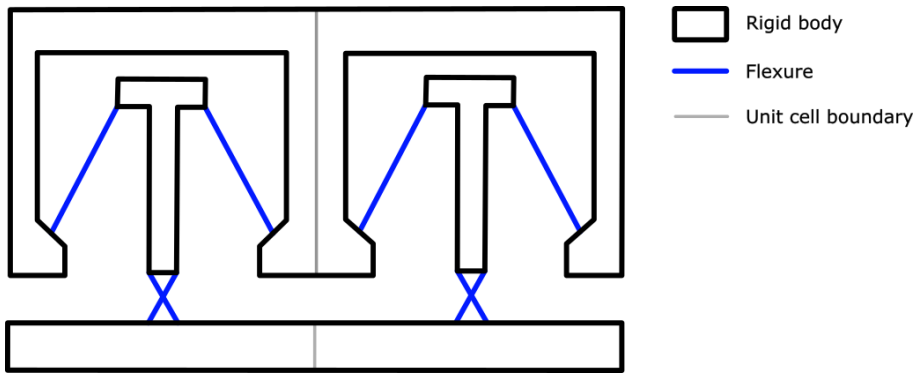

Figure 6: Two unit cells of Roberts mechanism, each having two leaf springs and a cartwheel.

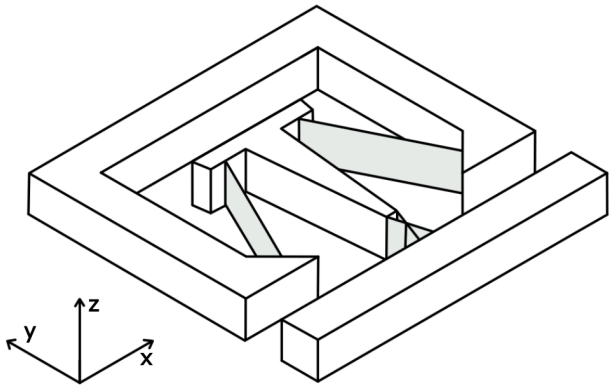

Figure 7: Isometric sketch of the unit cell, showing the convention for the x, y and z directions. The flexures are colored in grey.

2.2.2 Analytical model unit cell

In this section the analytical models for the parameters are explained. First the degree of freedom (DoF) is presented, resulting in the stiffness K_x, maximum force F_x, flexure stress and translational crosstalk. The analysis is continues with the out of plane stiffness K_z and the in plane constraint stiffness K_y.

The model for the DoF uses a Pseudo-Rigid-Body Model (PRBM)[17]. Here the kinematics are derived from rigid links and revolute joints. The kinetics are derived from torsional springs at the revolute joints. The PRBM is shown in Figure 8a, with joints 1 through 4 originating from the leaf springs and joint 5 originating from the cartwheel. For initial modelling, the link lengths from Wan and Xu [26] are used. This results in the correct dimensions for approximate straight line motion, and allows validating the intermediate stiffness results. After this validation, the dimensions are adapted for 3D printing.

The PRBM assumes that the output link is horizontal, causing joint 5 to rotate during deformation. As the unit cell is tessellated to form a metamaterial, this assumption is reasonable. Additionally, joints 1 and 4 are rigidly connected the base, assuming the frame is infinitely stiff.

To calculate the output displacement and link angles, two vector loops are required. Vector loop 1 is used to calculate the joint angles of the four bar mechanism, Figure 8a, and vector loop 2 is used to calculate the output displacement, Figure 8. The link angles are taken from positive x axis to vector $\vec{r_i}$ and the vector sum is considered clockwise. The summations are shown in Equation 1 for vector loop 1 and Equation 2 for vector loop 2.

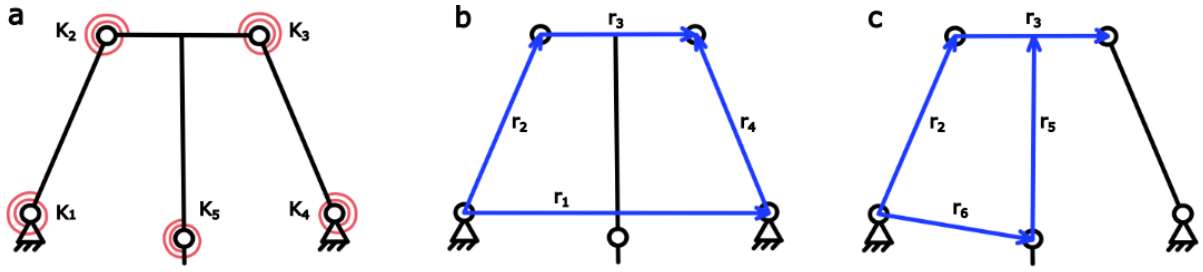

Figure 8: Pseudo rigid body model and vector loops for Roberts linkage (a) PRBM (b) Vector loop 1 (c) Vector loop 2

$$\vec{r_1} + \vec{r_3} - \vec{r_4} - \vec{r_1} = \vec{0} \tag{1}$$

$$\vec{r_2} + \frac{1}{2}\vec{r_3} - \vec{r_5} - \vec{r_6} = \vec{0} \tag{2}$$

In subsection 6.1 the vector loop equations are solved. The unknown angles for vector loop 1 are θ_3 and θ_4. The results are shown in Equation 3 and Equation 4. Vector $\vec{r_3}$ and vector $\vec{r_5}$ are connected to form the coupler link, therefore θ_5 is rotated 90° with respect to θ_3. Having the link angles allows calculation of vector loop 2, with unknown length L_6 and angle θ_6. The results are shown in Equation 6 and Equation 5. The expression for L_6 contains a cosine in the denominator, resulting in a possible division by zero. However, θ_6 does not reach multiples of 90 degrees in the operating range and therefore the cosine never becomes zero. Having the

output vector allows taking the x and y components of the output displacement of joint 5. Simple geometry gives Equation 7 and Equation 8.

$$\theta_3 = cos^{-1}\left(\frac{L_4 cos(\theta_4) - L_2 cos(\theta_2) + L_1}{L_3}\right) \tag{3}$$

$$\theta_4 = 2tan^{-1}(t) \; with \; t = \frac{-B - \sqrt{B^2 - AC}}{A} \tag{4}$$

$$\theta_6 = tan^{-1}\left(\frac{L_2 sin(\theta_2) + \frac{1}{2}L_3 sin(\theta_3) - L_5 sin(\theta_3 + 90°)}{L_2 cos(\theta_2) + \frac{1}{2}L_3 cos(\theta_3) - L_5 cos(\theta_3 + 90°)}\right) \tag{5}$$

$$L_6 = \frac{L_2 cos(\theta_2) + \frac{1}{2}L_3 cos(\theta_3) - L_5 cos(\theta_3 + 90°)}{cos(\theta_6)} \tag{6}$$

$$x = L_6 cos(\theta_6) \tag{7}$$

$$y = L_6 cos(\theta_6) \tag{8}$$

The actuation force is derived using virtual work and Freudenstein's kinematic coefficients[17]. The general formula for virtual work of a PRBM is shown in Equation 9. Where K_i are the rotational stiffnesses of the PRBM, following the flexure types, and ϕ_i are the relative angles between the links. For joints 1 through 4 the leaf spring stiffness is Equation 10[17] and joint 5 is the cartwheel shown in Equation 11[28][27]. The resulting expression for F_x is long and will be calculated in python, where the different functions are combined. An intermediate result for F_x is shown in Equation 12, giving rise to the kinematic coefficients $\delta\theta_i/\delta\theta_j$[17].

$$F\delta x = \sum_i K_i \phi_i \delta\phi_i \tag{9}$$

$$K_{leaf} = 2\gamma K_\Theta EI/L \tag{10}$$

$$K_{cartwheel} = 8EI/L \tag{11}$$

$$F = \frac{1}{\frac{D\delta\theta_2 + E\delta\theta_3}{A\delta\theta_2}} + \frac{1}{\frac{D\delta\theta_2 + E\delta\theta_3}{B\delta\theta_3}} + \frac{1}{\frac{D\delta\theta_2 + E\delta\theta_3}{C\delta\theta_4}} \tag{12}$$

To calculate the RoM, the flexure stress is used. The RoM is determined by the displacement where the flexure stress reaches the yield stress. For practical applications the mechanism requires a safety factor for suitable fatigue life, however for analysing the change in behaviour the yield stress is sufficient. For the approximation of a fixed-fixed beam, the flexure stress of a fixed-guided beam is used[17]. The formula's for load and stress are shown in Equation 13 and Equation 14. The adaptation changes parameter a, where the expression includes both θ_2 and θ_3 (shown in subsection 6.1.

$$P = \frac{4K_\theta EI\theta}{L^2 cos(\theta)} \tag{13}$$

$$\sigma_{max} = \frac{Pac}{2I} \tag{14}$$

The constraint stiffnesses are derived in subsection 6.1, using beam equations for the leaf springs. The stiffness in z direction is calculated by translating the force to the output of the flexure, giving rise an additional moment load. For simplification it is assumed that the additional deflection at the cartwheel is negligible, therefore link 5 is modelled as a rectangular beam. The beam equations are summed and rewritten to obtain Equation 15. Similarly the stiffness in y direction is derived, where the force is translated to compression and bending loads, resulting in Equation 16.

$$K_z = 2\frac{F}{\delta z} = \frac{2}{\frac{L}{EI}\left(\frac{L^2}{3} - \frac{rL}{2} - \frac{rLcos(15)}{2} + r^2 cos(15)\right) + \frac{r^2 sin(15)L}{GJ_T}} \tag{15}$$

$$K_y = \frac{3EI}{L^3}\frac{EA}{L} \tag{16}$$

2.2.3 Initial unit cell validation

For the initial validation, dimensions of Wan and Xu [26] are used. The analytical model results in the output trajectory of Figure 9a, which is similar to the literature of Figure 4a. The figure includes the maximum range of 7 mm, which is limited compared to the straight line section. This allows increasing the RoM during the main research.

The analytical and FEM results are compared to validate the models. For this the geometry is generated in SolidWorks and imported as parasolid(.X_T) into Ansys Workbench. The material is selected as AL-7075, after which the model is meshed. The bases of the leaf spring are constrained with a fixed support and the output displacement is applied to the tip of the coupler link. For analysis it is important that the large deflection setting is turned on.

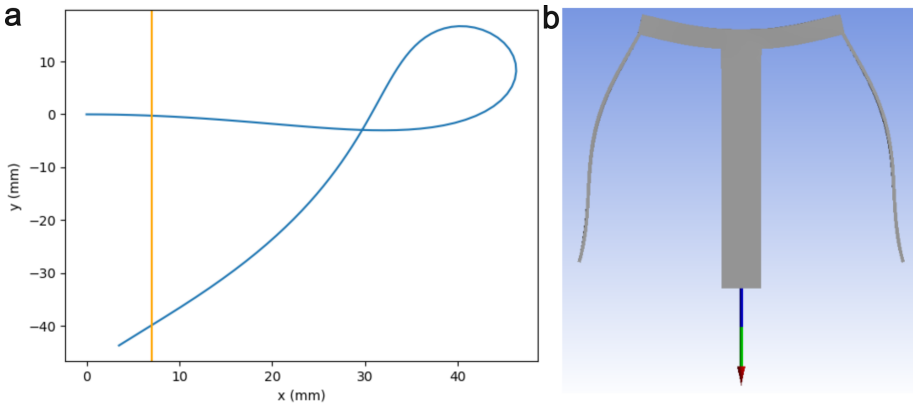

Figure 9: (a) Output trajectory of the analytical model, showing the RoM of 7 mm in orange (b) FEM result for deformation in y direction

The reference design composes of eight parallel mechanisms. The obtained force of 160 N is therefore divided by eight and divided by the displacement of 7 mm, resulting in a stiffness of 2.86 N/mm. This value aligns well to the analytical model and initial FEM simulation for the DoF, as seen in Table 3. The constraint stiffness is validated between the FEM and analytical models, similarly shown in Table 3. The approximation using beam equations is fairly close to the FEM result. However, the stiffness in y direction differs in magnitude. The analytical model assumes compression and bending, whereas the FEM result shows deformation that resembles buckling, shown in Figure 9b. For the relative behaviour, and high stiffness compared to the other two stiffnesses, the result is sufficient. With the intermediate results validated, the models can be adapted for the main analysis.

Table 3: Initial stiffness results for the reference dimensions

Stiffness (N/mm)	K_x	K_y	K_z
Analytical	2.78	11600	147
FEM	2.75	3380	129

2.3 Analytical modelling

To model the effect of an m x n configuration of unit cells, the analysis is divided into distinct components. First the number of unit cells is presented, with parallel unit cells denoted by m and series unit cells by n. Additionally, both parallel and series arrangements are analysed with a focus on maintaining constant DoF stiffness. Finally, the scale of the unit cell is derived using the formula's for the various parameters of interest.

2.3.1 Parallel

Parallel unit cells are connected by joining both the C-shaped frames and the output links of the adjacent unit cells. Figure 10 shows the convention for parallel unit cells. The bottom of the unit cells, where the C-shaped frame resides, is connected to ground. The top of the unit cells share the actuation force, as all output links are connected.

This configuration causes the deformation of the structure to equal the deformation of the individual unit cells. In simple compression or extension springs, each spring moves the same amount and therefore the overall stiffness is the sum of the individual stiffnesses. For the shear cell, it is expected that the stiffnesses and

maximum force similarly add. Since each unit cell is identical, the sum over m unit cells can be represented by multiplication of factor m. This multiplication assumes that the connection between unit cells will not interfere with the behaviour of the unit cells, which is discussed in section 4.

As each individual unit cell is deformed equally, the resulting stress is equal for each unit cell. Therefore having a constant RoM. This constant RoM results in a constant translational crosstalk between the x and y directions.

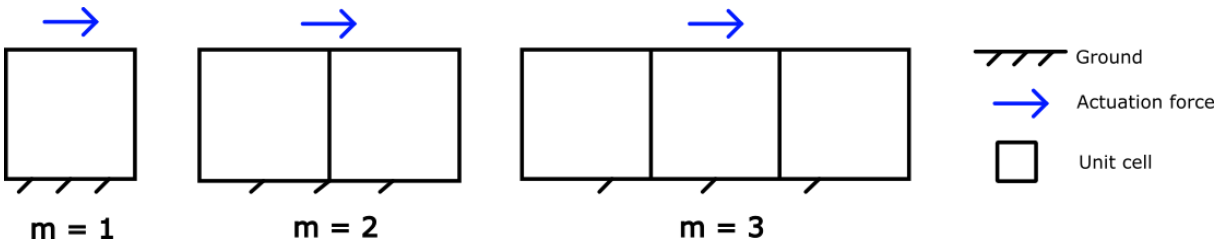

Figure 10: Parallel configuration with one to three unit cells

2.3.2 Parallel with Scaling

All stiffnesses of parallel unit cells are expected to increase with factor m, meaning a constant stiffness ratio. However, applications could require a low actuation force. For situations where $m > n$ and no additional stiffness is desired, the thickness of the flexures is adjusted maintain constant DoF stiffness.

As seen in subsection 6.1, $K_x \propto \frac{Ewt^3}{L^3}$. Therefore to keep the stiffness the same for an increase with m, the thickness is multiplied by a factor of $\sqrt[3]{\frac{1}{m}}$. This also increases the RoM, as stress is proportional to $\frac{t}{L}$, reaching the yield stress at a larger displacement. The flexure stress is not linear but slowly increasing in magnitude, therefore the increase in RoM is expected just below factor $\sqrt[3]{m}$.

The new geometry is computed in a python loop, resulting in the new stiffnesses, force, RoM and translational crosstalk for the unit cell. Combined with the multiplication factors of parallel unit cells results in the characteristics of the overall structure. The maximum force and translational crosstalk increase accordingly, as they are dependent on the RoM.

Adjusting the thickness of the flexures allows the trade-off between RoM and stiffness. For more parallel unit cells compared to series unit cells, this could increase the RoM. However, the compactness is not increased as the RoM increases with $\sqrt[3]{m}$ but the volume increases with m. For applications where the design volume is narrow, this method could still allow a bigger RoM compared to equal number of series and parallel unit cells, while maintaining the same stiffness.

2.3.3 Series

Series unit cells are connected by joining the output link of the previous unit cell to the C-shaped frame of the next unit cell. The convention for series stacking is shown in Figure 11. Here only the first unit cell is connected to ground and only the last unit cell is actuated. For the chosen unit cell, where rotation is constrained by parallel stacking, the geometry constrains the rotation from m = 2. For analysis 3 x n is chosen to constrain the rotation, having rows instead of individual unit cells.

Compression or extension springs in series have a constant internal force, while the deformation adds up. The equivalent stiffness is the series sum of all the individual springs, computed as Equation 17. For the analytical model it is still assumed that the rotation of the unit cell is appropriately constrained, posing a requirement on the number of parallel unit cells. Therefore the DoF stiffness K_x and the DoC stiffness K_y are the series sum of the stiffnesses of the unit cells. With each unit cell having equal stiffness, the series sum is represented by multiplication by $\frac{1}{n}$. The RoM is the sum of the individual unit cells, represented by a multiplication factor n. The increase in RoM with factor n also translates to the translational crosstalk by the same factor. The DoF stiffness multiplied by the RoM results in a constant maximum DoF force.

$$K_{series} = \frac{1}{\frac{1}{K_1} + \frac{1}{K_2}} \tag{17}$$

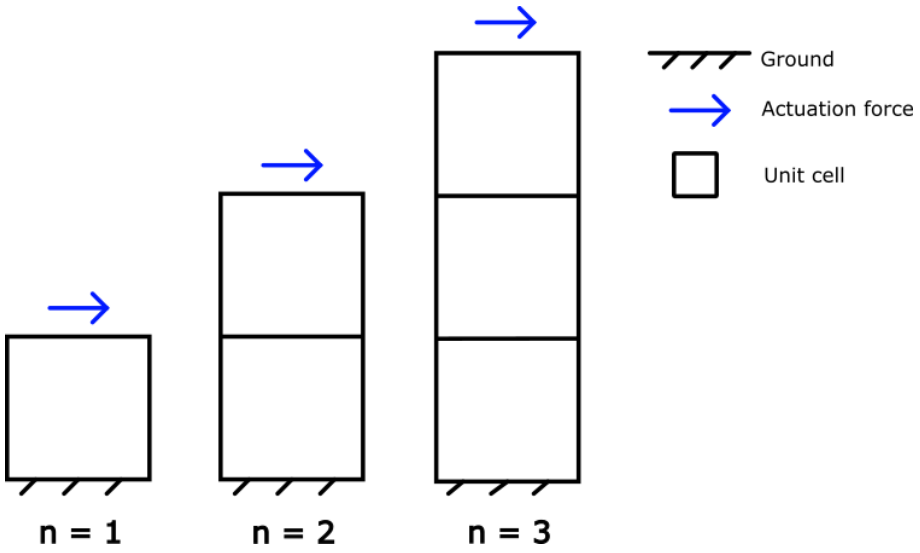

Figure 11: Series configuration with n from one to three

The out of plane stiffness, K_z, requires more extensive calculation. The distance to the external force induces an increasing internal moment between the unit cells, as illustrated in Figure 12. The nonuniform load disrupts the simple spring analogy, necessitating different calculation approach. In python the effective stiffness per unit cell is computed by varying the distance to the external force. This causes the first unit cell, fixed to the external environment, to have the lowest effective stiffness. The overall stiffness is calculated as the series sum of each effective stiffness. Due to the reduction in effective stiffness from increasing internal moment, the overall out of plane stiffness reduces at a higher rate compared to the in plane stiffnesses.

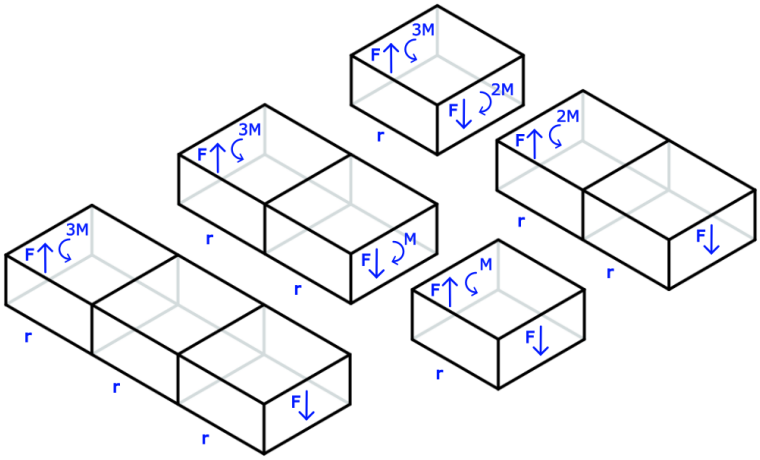

Figure 12: Free body diagrams showing the change in boundary condition for the series stacking of unit cells. The left unit cell is connected to a rigid base, resulting in reaction force F and moment $3M = 3rF$. The three attached unit cells have external force F applied at the free end. Separating one unit cell results in the same force F and moment rF on the second interface, as the original force is applied at distance r. Removing two unit cells shows an increase in moment to $2rF$, due to the distance of the applied force increasing to $2r$.

2.3.4 Series with Scaling

As seen in subsection 6.1, $K_x \propto \frac{Ewt^3}{L^3}$. Therefore to maintain constant stiffness for a decrease with n, the thickness is multiplied by a factor of $\sqrt[3]{n}$. This also decreases the RoM of the unit cells, as stress is proportional to $\frac{t}{L}$, reaching the yield stress at a smaller displacement. However, due to the added serial unit cells, the total RoM still increases. Linear approximation of the flexure stress results in a total RoM increase of $n\sqrt[3]{1/n} = n^{\frac{2}{3}}$.

In python, the adjusted flexure thicknesses are computed by factor $\sqrt[3]{n}$, resulting in the new unit cell characteristics. These characteristics are then multiplied or inserted in the calculation of K_z, as would be done with the original unit cell in series arrangement.

2.3.5 Scaling n x n unit cells

For the scale of the unit cell a square configuration of n by n unit cells is examined, as the series and parallel stiffness effects cancel. Dividing the length dimensions by $\frac{1}{n}$ yields approximately the same overall size, with minor variations from flexure thickness. This convention is shown in Figure 13, where n denotes the n x n tessellation. For scaling of the unit cell three different variations are examined. The most straightforward variation is scaling each parameter by the same scale factor $\frac{1}{n}$. The second variation is scaling the lengths and thicknesses by $\frac{1}{n}$, while maintaining constant out of plane thickness. Lastly only scaling the lengths by $\frac{1}{n}$.

In python the lengths, thicknesses and out of plane thickness are appropriately scaled with $\frac{1}{n}$, resulting in the unit cell characteristics. For the overall structure the parallel and series formula's are simultaneously applied.

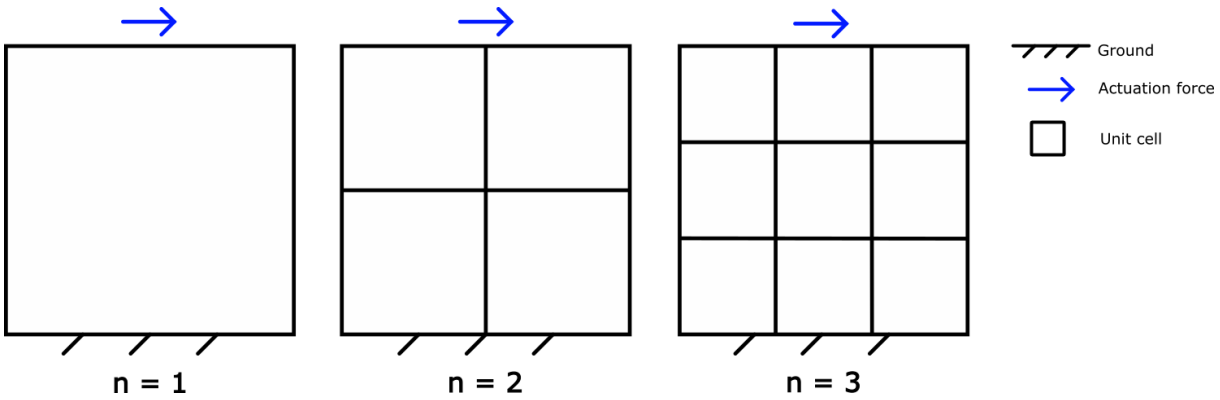

Figure 13: Sketch of n x n scaling, with n ranging from one to three. The unit cells are sized 1/n resulting in the same overall size.

Although the code requires minor adjustments, it is still essential to understand the expected behaviour. The formula's for the properties of interest, as derived in subsection 6.1, are reduced to be proportional to the relevant parameters. Scaling all relevant parameters results in equal unit cell stress, Equation 18, combined with scaled RoM per unit cell of $\frac{1}{n}$ and n from series arrangement gives constant RoM. In Equation 20 there is one more parameter in the numerator than the denominator, therefore the stiffness scales with $\frac{1}{n}$. The force, Equation 19, scales with $\frac{1}{n^2}$ for a unit cell or multiplied by n for the overall force $\frac{1}{n}$. Finally K_z scales with $\frac{1}{n}$ similar to K_x, but flexure thickness and out of plane thickness are exchanged.

$$\sigma_x \propto \frac{t}{L} \tag{18}$$

$$F_x \propto \frac{wt^3}{L^2} \tag{19}$$

$$K_x \propto \frac{wt^3}{L^3} \tag{20}$$

$$K_z \propto \frac{tw^3}{L^3} \tag{21}$$

From Equation 20, scaling for constant DoF stiffness can be derived, flexure thickness and length are both cubed. Thus, maintaining constant out of plane thickness results in constant in plane stiffness. The force per unit cell scales as $\frac{1}{n}$, however the overall force of the structure remains unchanged. Out of plane stiffness K_z increases with n^2, as thickness is divided by length cubed. Therefore, only scaling length and flexure thickness can compensate part of the reduction in K_z caused by the series arrangement.

The final approach involves only scaling the lengths, while maintaining the flexure thickness and out of plane thickness constant. This approach increases the stiffness by factor n^3, rendering it unusable for a motion system.

2.4 Finite Element Method

For both simulation and experiment the geometry is parametrically designed in SolidWorks, enabling tessellation and scaling. The geometry is saved as parasolid (.X_T) file extension and imported into Ansys workbench. The Static Structural module is used to simulate the quasi-static load conditions, combined with large deflection

turned on. The material selected for 3D printing is PETG[29], which is well suited for compliant mechanisms. The flexural modulus, Young's modulus measured in bending[30], is $E = 2.1GPa$[29] and the Poisson's ratio is $\nu = 0.35$. The yield stress is $\sigma_{yield} = 51MPa$.

To illustrate how the mesh and boundary conditions are applied, a sample of 3 by 3 unit cells is shown in Figure 14. To control the size of the mesh Ansys standard meshing resolution is used for the rigid bodies, as these have small deformations and stress. The flexures have highly concentrated deformations and therefore need to be refined. For the mesh refinement, the flexure surfaces are selected as shown in Figure 14a. The selection includes part of the rigid body, which is avoided by multi body simulation. Multibody simulation allows for better mesh control in the thickness direction, improving the stress as verified in subsubsection 6.3.3. However, this leads to additional bonding constraints, resulting in varying results. Apart from stress the effect is negligible, therefore it is chosen to use a single body for the simulations. In subsubsection 6.3.2 a convergence study is carried out, resulting in the desired mesh size of 24 subdivisions per leaf spring. Figure 14b shows the resulting mesh, which is relatively coarse at the low deformations and very fine at the flexures. The element type selected by Ansys is SOLID187[31], which is a quadratic element that is well suited for irregular mesh and large deformations.

To simulate the sample, the base is fixed by applying a fixed surface shown in blue in Figure 14c. To actuate the output link, a displacement is applied to the orange surface in Figure 14c. The deformation for stiffness calculation is set to 0.1 mm in each direction and to the calculated RoM for the maximum force and crosstalk. Probing the deformation verifies that the applied displacement is correct and is used for stiffness calculation. The reaction force of the displacement is probed, providing the force in all three directions. In excel the force is divided by displacement, resulting in stiffness. For the translational crosstalk a small surface is probed for y displacement, in the center for the output link. For rotational crosstalk, the outside faces of the output link are used, as shown in green in Figure 14c. From the excel file, the data is copied to the correct python script to analyse the results.

For n by n scaling analysis, the mesh results in high numbers of nodes. Therefore only n is 2, 4 and 6 are simulated. The other scaling results are obtained by simulating the unit cell alone. Next to this, the element size for the flexures and the displacement for calculating the stiffness are scaled accordingly. For the first parallel data-point and the scaling of unit cells a different setup is used. The output face is constrained with a remote displacement, with rotation along the z axis set to zero. This ensures consistent behaviour to the analytical model and the rest of the samples, where the rotation is constrained.

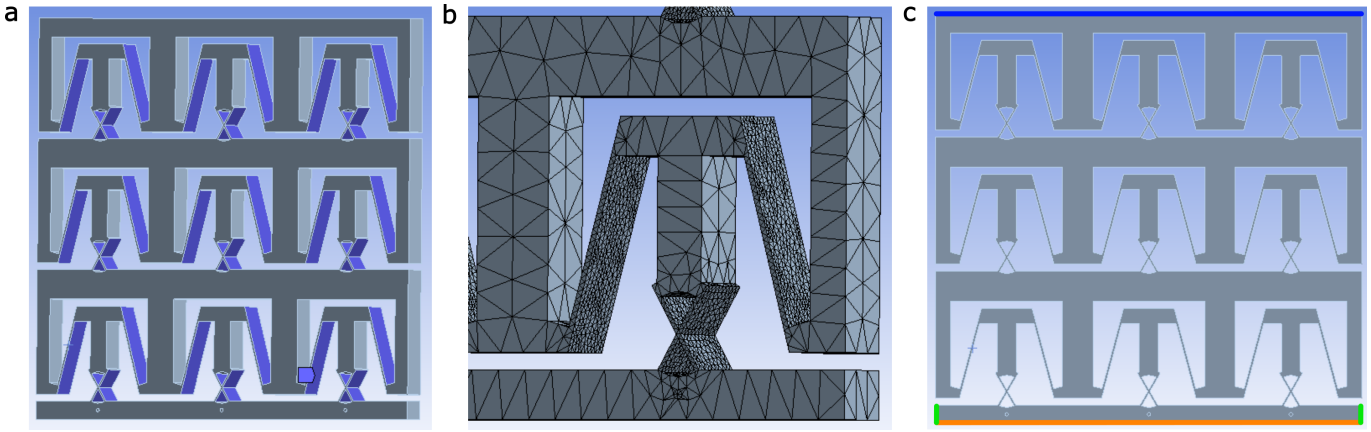

Figure 14: FEM setup (a) flexure faces selected for element sizes, (b) resulting mesh for one unit cell and (c) the boundary conditions for analysis. The blue line is the fixed surface, orange the actuation and displacement probe and green the faces for measuring crosstalk rotation. The cylinders on the output link, at the bottom, provide the average crosstalk in the center and a another measure for rotation.

Typical results are shown in Figure 15. Figure 15a shows the total deformation at RoM, illustrating the deformation of the unit cells and the translations and rotation of the output link. It is observed that the output link rotates, therefore this result is also evaluated. Figure 15b shows the stress distribution, where the maximum stress is localised at the location of joints 2 and 3 of the PRBM in Figure 8a.

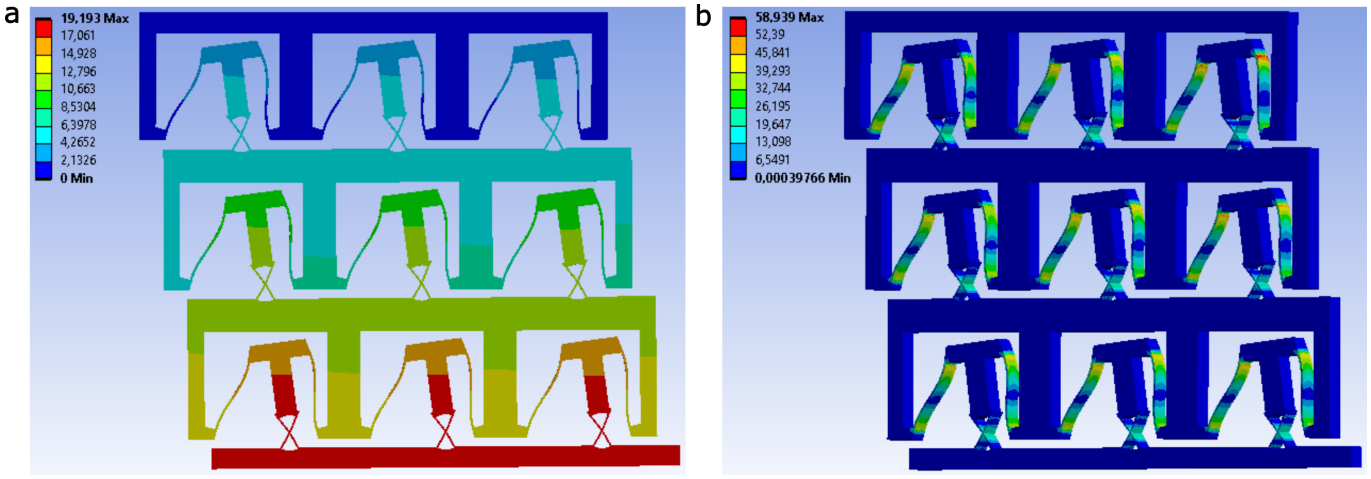

Figure 15: The typical results for the FEM simulations, showing (a) total deformation in mm and (b) equivalent stress in MPa

2.5 Experiment

Each variation was tested using configurations of m or n unit cells, with values of 2, 4 and 6. The characteristics of stiffness, maximum force and crosstalk (translation and rotation) are experimentally validated. Each setup uses a PI motion stage for displacement and a force sensor at the output of the PI motion stage. The system is actuated using a LabVIEW program, tailor made for the actuator and sensor combination. The data is exported into excel for later analysis in python. Using a combination of stepped blocks and allthread, components are locked in place.

The samples are 3D printed on a BambuLab X1C, in PETG material. For parallel, series and series with scaling, a 0.4 mm nozzle is used. The number of walls is set to 3, combined 25% gyroid infill. Gyroid infill produces a circular mesh, having near isotropic behaviour. The samples for parallel with scaling and scaling are produced with a 0.2 mm nozzle, as the flexures decrease in thickness. The number of walls is 4 and similar 25% gyroid infill is used. It is important to remove seams on the thin flexures, further explained in subsubsection 6.4.1.

The experiments are repeated five times to average the results. The first measurement is discarded as conditioning of the PETG can occur. Conditioning shows large hysteresis in the first measurement, after which the results are closely aligned. In python the measurements are separated into the different measurement runs and two points are picked to calculated the stiffness or a single point for the force. Visually it is inspected if the points align to the expected locations on the graph, after which the data is saved and imported to the desired python files.

The stiffness in y direction is measured by compressing the sample, as shown in Figure 16. An aluminium box profile, 15x15x1.5mm, is clamped to represent the fixed surface constraint. The base link is clamped to an aluminium H-profile, 9.1x12x6.5x1.3 mm, to increase the stiffness of the actuated link. At one side of the sample, a clamp and allthread combination is used to hold it in place. For the samples showing low out of plane stiffness, a stepped block is placed under the sample to compensate gravity and align the sample to the actuation point. The PI stage is pushed against the aluminium H-profile, which results in a reaction force. The wider samples show an initial gap, gradually closing at small displacements. Therefore, the upper range of data is used for calculating the stiffness.

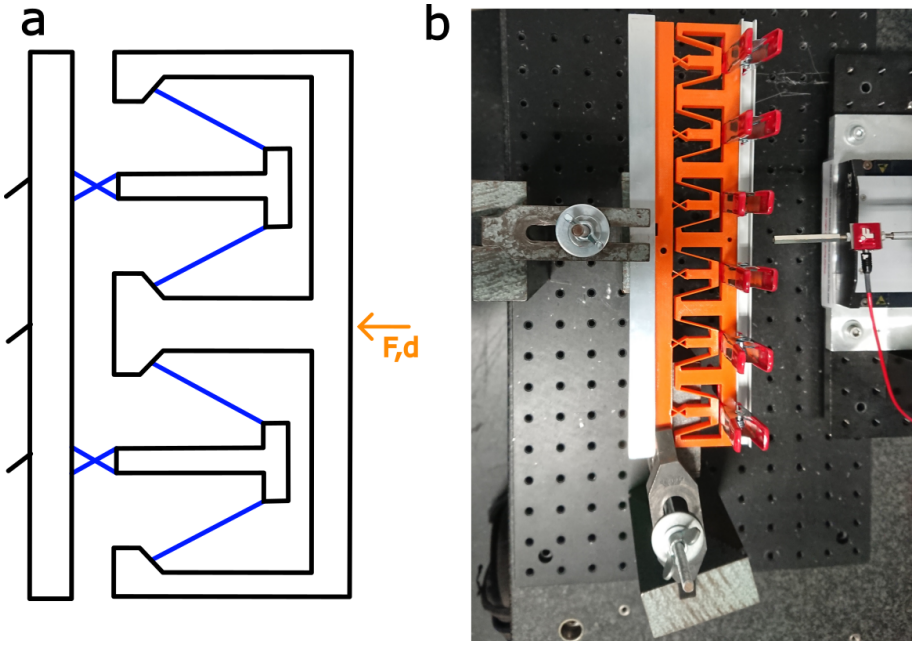

Figure 16: Setup for measuring K_y, (a) sketch and (b) the real setup

The z direction measurements are similar in actuation and sensing as the y direction. The clamping is realised in two ways. Figure 16b shows two blocks clamped on the base plate. Here the parallel samples are clamped vertically to the blocks, using metal hand screw clamps. The wider samples have an additional stepped block in the center, constraining the rotation (about the x axis) at the center of the sample. Figure 16c shows the setup for the taller samples, which are tested horizontally. Here the stepped blocks are taller, allowing tree metal hand clamps to properly constrain the edges and center of the samples. Having the samples constrained, the PI stage pushes the sensor, connected to a bolt, onto the center of the output link. The reaction force and displacement for K_z are identically analysed as K_y

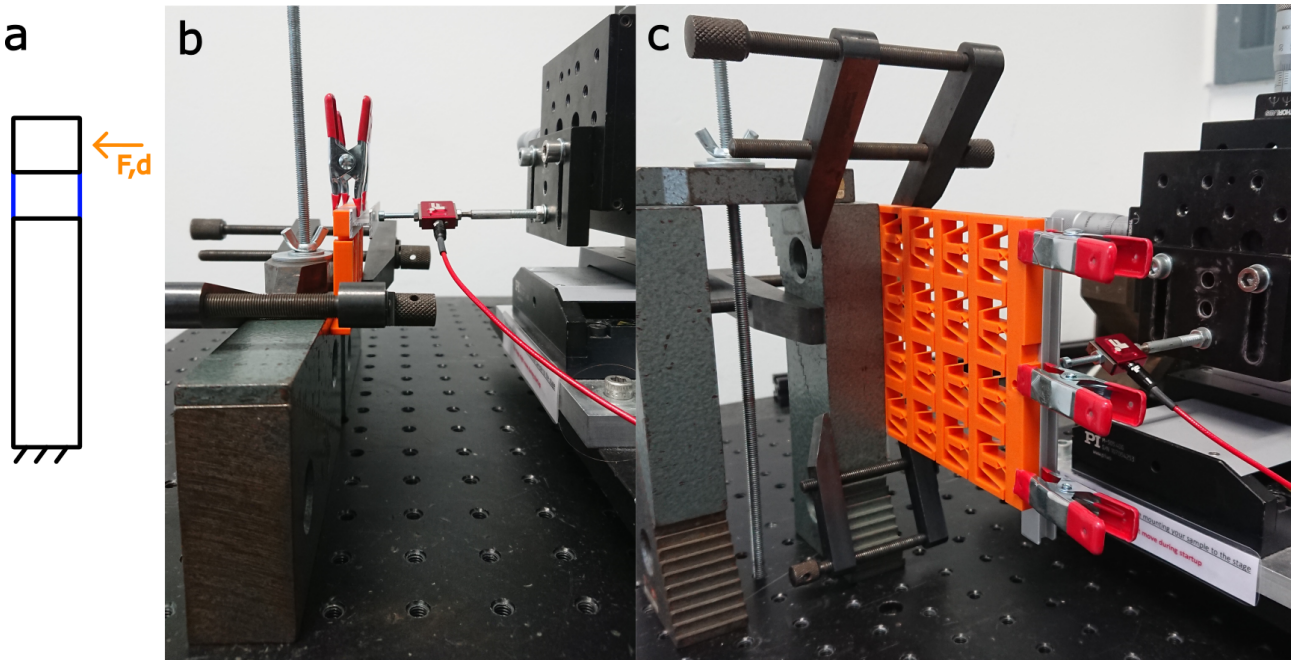

Figure 17: Setup for measuring K_z, (a) sketch, (b) setup for parallel and (c) setup for series and scaling

The setup for the DoF is more elaborate, and illustrated in Figure 18. Here the output link is mounted to an aluminium linear guide mechanism, also based on Roberts linkage. The constraint for the base link is modelled as a slider with a pivot, allowing one rotation and one translation. This is approximated by a two

long iron wires, formed into a link with two revolute joints at the ends. The links are free to rotate around a bolt, mounted to the sample and fixed to an aluminium Thorlabs profile using another 3D print. The PI stage pulls the output link linearly, recording the force required. This displacement causes the crosstalk at the base link, equivalent to fixing the base and allowing motion at the output link. This crosstalk is measured using a Keyence laser displacement sensor, at the center and 50 mm to the left. Crosstalk is manually logged into excel, where the average and standard deviation are also calculated. The actuation force is analysed by taking the maximum of the run for the maximum force, and taking two points along the curve to divide the difference in force by the difference in displacement.

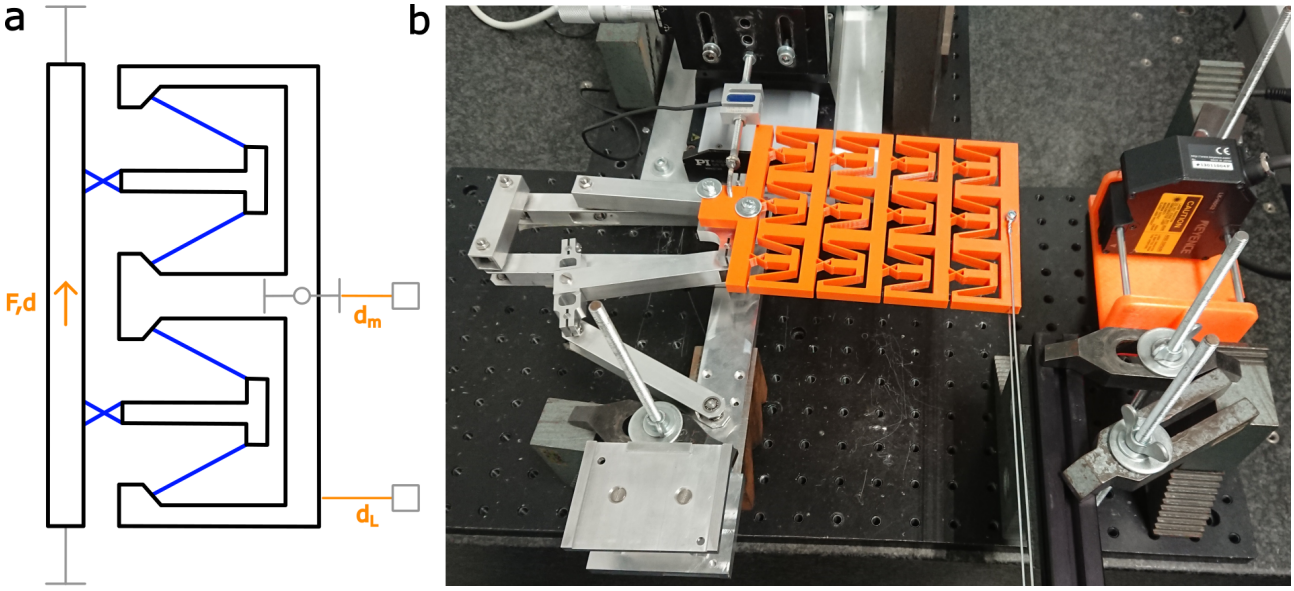

Figure 18: Setup for measuring K_x, (a) sketch and (b) the real setup

3 Results

This section presents the results for parallel, series and scaling configurations. The graphs include the analytical prediction, the FEM simulations and the experimental results. Data points are represented by continuous lines for analytical predictions, circular markers for FEM simulations, and circular markers with error bars indicating the mean and standard deviation for experimental results. Each subsection begins with the calculated RoM, followed by the DoF stiffness, maximum force, the DoC stiffness and lastly the crosstalk. For parallel scaling and series scaling the stress in the leaf spring is also illustrated to explain the change in RoM. The dimensions for each variation are shown in subsection 6.2

3.1 Number of unit cells

The following subsections present the results for the behaviour change caused by the number of unit cells. The overall size of the unit cell remains constant.

3.1.1 Parallel

The predicted RoM for parallel unit cells is constant at 6.38 mm, therefore the graph is omitted.

The results for the DoF, presented in Figure 19, show perfect linear behaviour. Both the stiffness and maximum force increase linearly with factor m. The experimental results are higher in magnitude, which is explained in section 4.

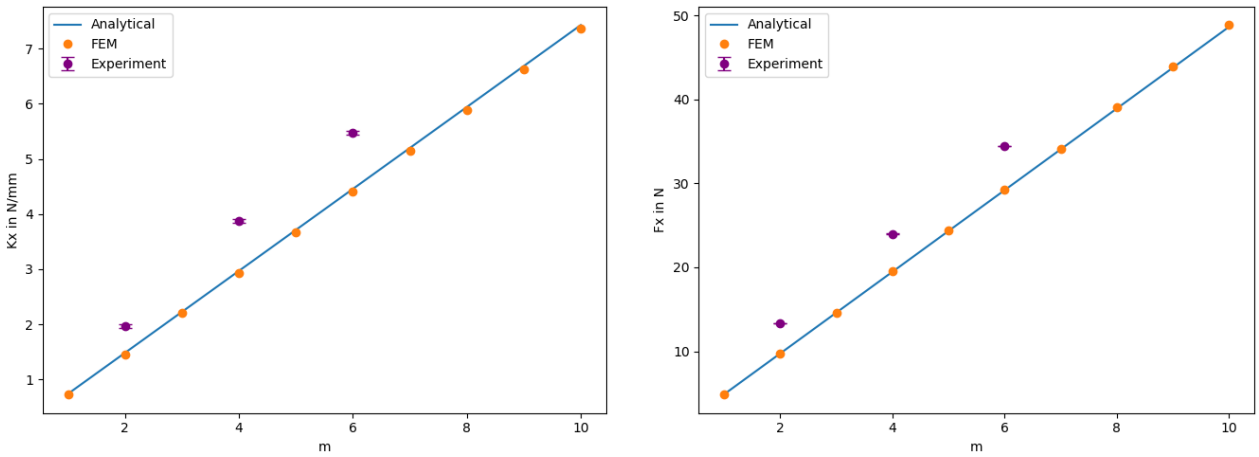

(a) Stiffness in x direction

(b) Force at maximum range

Figure 19: DoF results parallel unit cells

Figure 20 shows the DoC stiffness, expected to increase linearly with m. As shown in Figure 20a, the FEM and experimental results are smaller in magnitude. Interestingly, the FEM model increases at a higher rate than linearly with factor m, which is explained in section 4. The stiffness K_z shows good agreement between the analytical and FEM results, only differing in magnitude. The experimental results however show a lower rate than predicted, which is also explained in section 4.

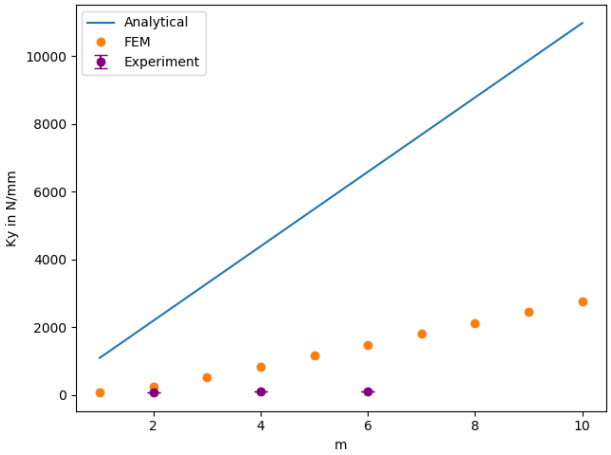

(a) Stiffness in y direction

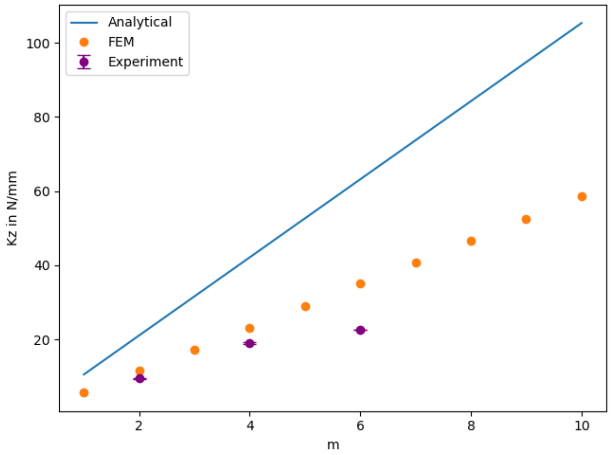

(b) Stiffness in z direction

Figure 20: DoC results parallel unit cells

As predicted, the translational crosstalk for the analytical and FEM models are constant in Figure 21a. The experimental results are not reliable for this set of measurements, and will not be discussed in detail. The rotational crosstalk of Figure 21b shows new behaviour. Similar to translational crosstalk, the rotational crosstalk of experiment is insufficient to describe behaviour. The FEM results show a decrease of $\frac{1}{m}$ in rotation by increasing the number of parallel unit cells. The exception to this is $m = 1$, which had the rotation constrained by remote displacement.

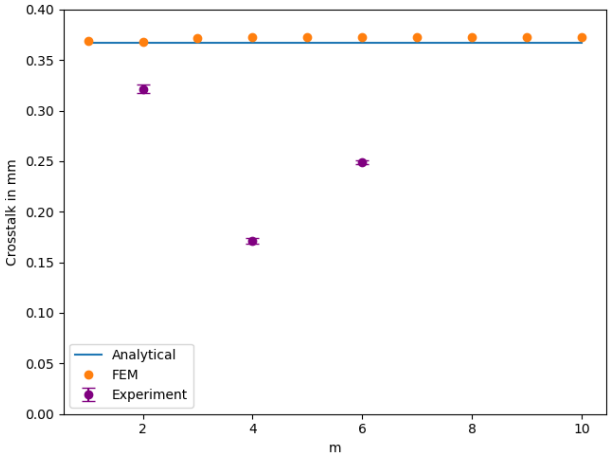

(a) Crosstalk x to y translation

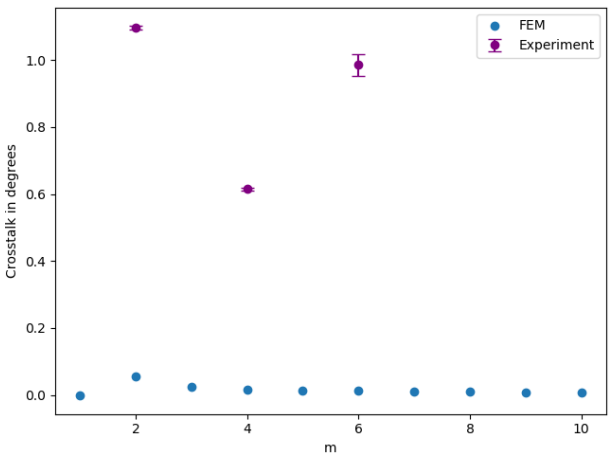

(b) Crosstalk x to in plane rotation

Figure 21: Crosstalk results parallel unit cells

3.1.2 Parallel with scaling

Figure 22a illustrates the working principle for extending the RoM. The stress decreases as number of unit cells increases, with flexure thickness reduced to maintain constant stiffness. The yield stress is reached at a larger displacement, increasing the RoM. The resulting RoM is also plotted against the number of unit cells in Figure 22b, showing a close match with derived factor $\sqrt[3]{m}$.

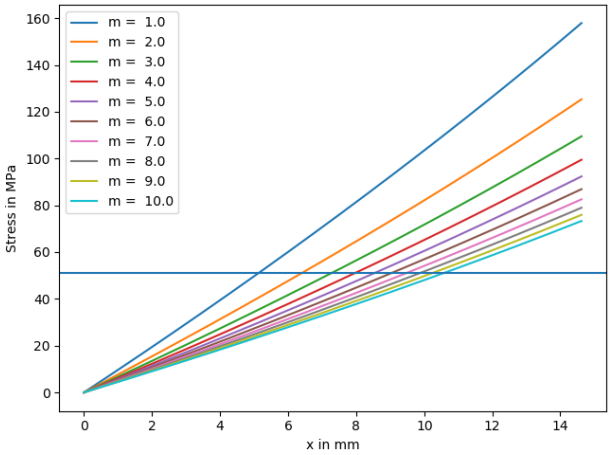

(a) Flexure stress versus x displacement.

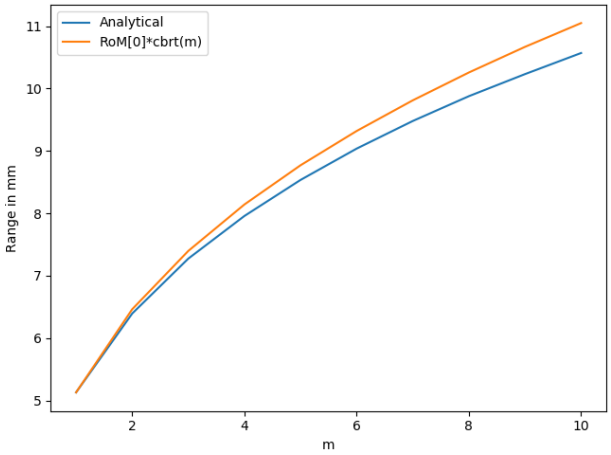

(b) RoM parallel scaling

Figure 22: Stress plotted versus displacement and RoM for parallel scaling, showing a close match to the predicted increase with $\sqrt[3]{m}$ in b. More parallel units have more slender flexures, therefore the intersection between flexure stress and the yield stress occurs at a larger displacement in a.

Figure 23a shows the stiffness K_x for both the unit cell and the overall structure. To maintain constant overall stiffness, the stiffness per unit cell is decreased with factor $\frac{1}{n}$. The FEM results show a slight increasing trend, however overall the data shows a good match with analytical results. The experiment does not present a clear trajectory. The overall force is increasing in Figure 23b, as the stiffness is maintained constant but the displacement is increased. Similar to stiffness, the FEM results show an increasing deviation from the analytical model.

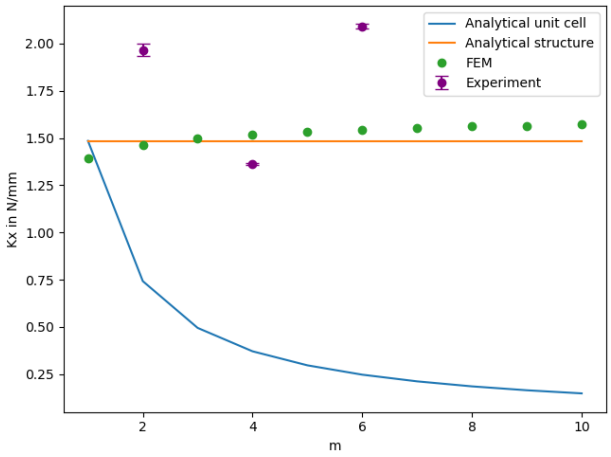

(a) Stiffness in x direction

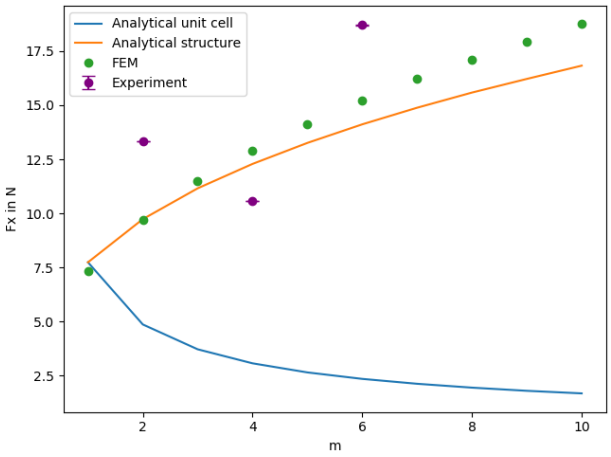

(b) Force at maximum range

Figure 23: DoF results parallel unit cells with changing flexure thickness

The analytical models for DoC stiffness differ in magnitude compared to the FEM model and experiment. Although the magnitude is different, both stiffnesses in Figure 24, show a similar trend to the analytical model. The stiffnesses of the unit cell decrease, while the overall stiffness increases.

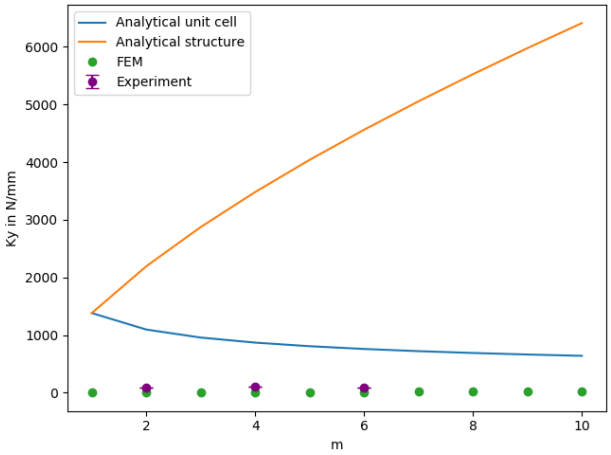

(a) Stiffness in y direction

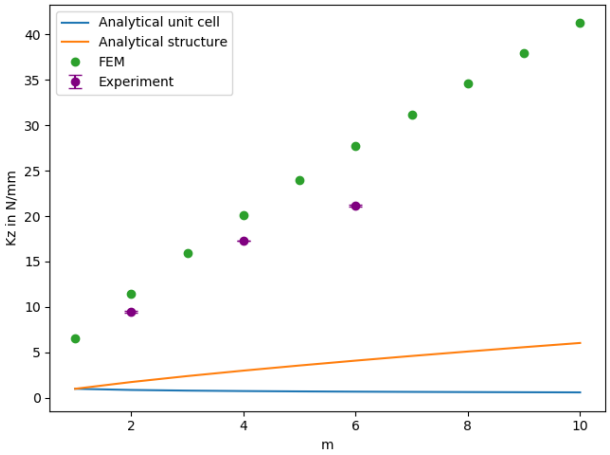

(b) Stiffness in z direction

Figure 24: DoC results parallel unit cells with changing flexure thickness

As the RoM is increased, the crosstalk also increases. Figure 25a demonstrates a similar trend in crosstalk to that observed for RoM in Figure 22b. Both the FEM model and experiment illustrate a similar tend, although the experimental results increase at a lower rate. The rotational crosstalk in Figure 25b shows a similar trend to the regular parallel results, reducing proportional to $\frac{1}{n}$. The experimental results are consistent with the parallel results, not showing a clear trend.

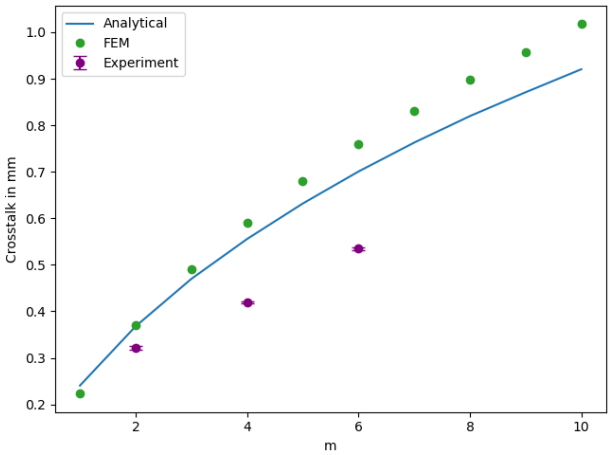

(a) Crosstalk x to y translation

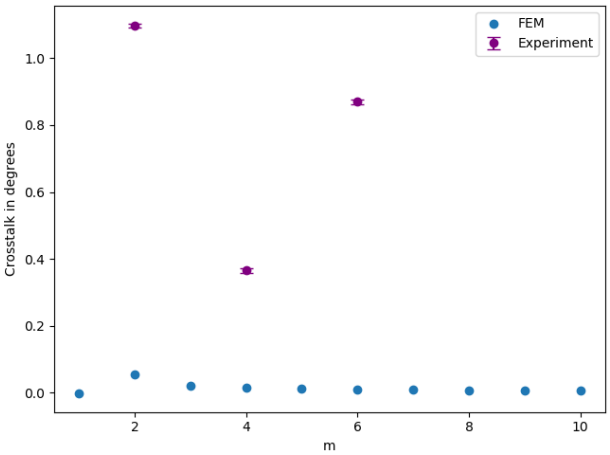

(b) Crosstalk x to in plane rotation

Figure 25: Crosstalk results parallel unit cells with changing flexure thickness

3.1.3 Series

The series results presented are derived for 3 x n unit cells. As stated in subsubsection 2.3.3, the RoM is linearly increasing with n.

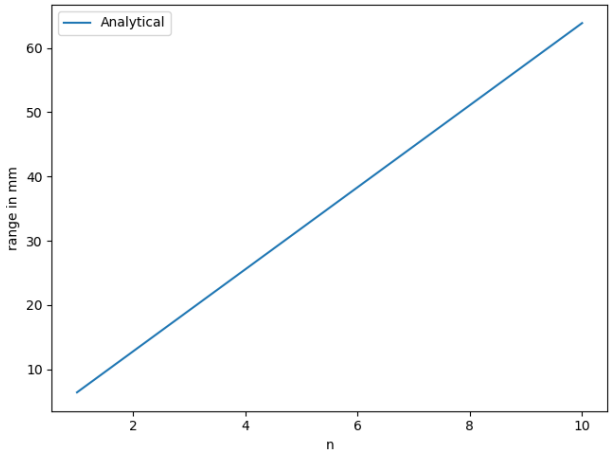

Figure 26: RoM for series, showing a linear increase with n.

Figure 27a shows DoF stiffness for the analytical and FEM models decreasing proportional to $\frac{1}{n}$. The Experimental results show a similar trend, although much lower in magnitude. The maximum force however, differs between analytical and FEM models. Figure 27b shows a constant analytical force, whereas the FEM model shows a decreasing force. The large deformations show a decrease in force due to the increasing rotation, which is further discussed in section 4. The experimental results share the decrease in magnitude, although the overall magnitude is significantly lower.

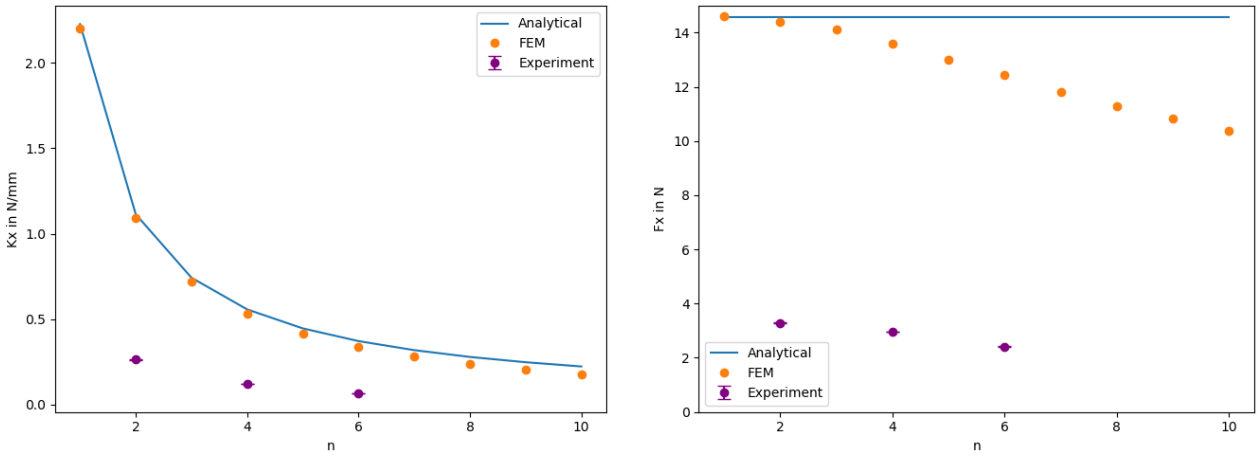

(a) Stiffness in x direction

(b) Force at maximum range

Figure 27: DoF results series tessellation

Figure 28a shows stiffness K_y decreasing proportional to $\frac{1}{n}$, although at different magnitudes across the different data sets. The out of plane results in Figure 28b demonstrate a close match among the models, each showing a rapid decrease as n increases.

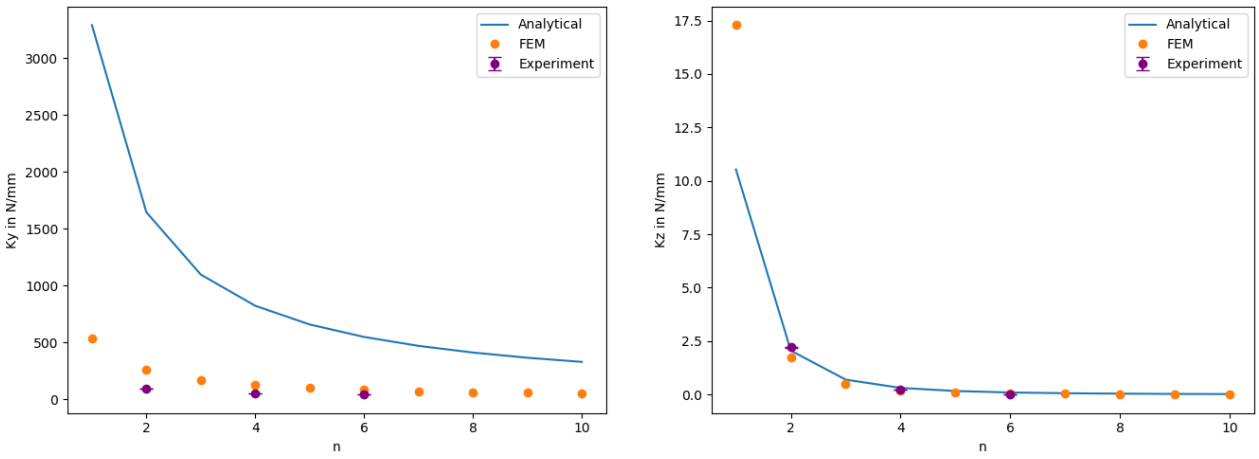

(a) Stiffness in y direction

(b) Stiffness in z direction

Figure 28: DoC results series tessellation

Figure 29a shows a linear increase for the translational crosstalk of the analytical model. Similar to the maximum force, the magnitude decreases with increasing n. The rotation effect is further discussed in section 4. The experimental results show a more significant decrease in magnitude compared to the FEM results. The rotational crosstalk is observed to increase with increasing n, as shown in Figure 29b. The experimental results show a similar increase at a higher magnitude.

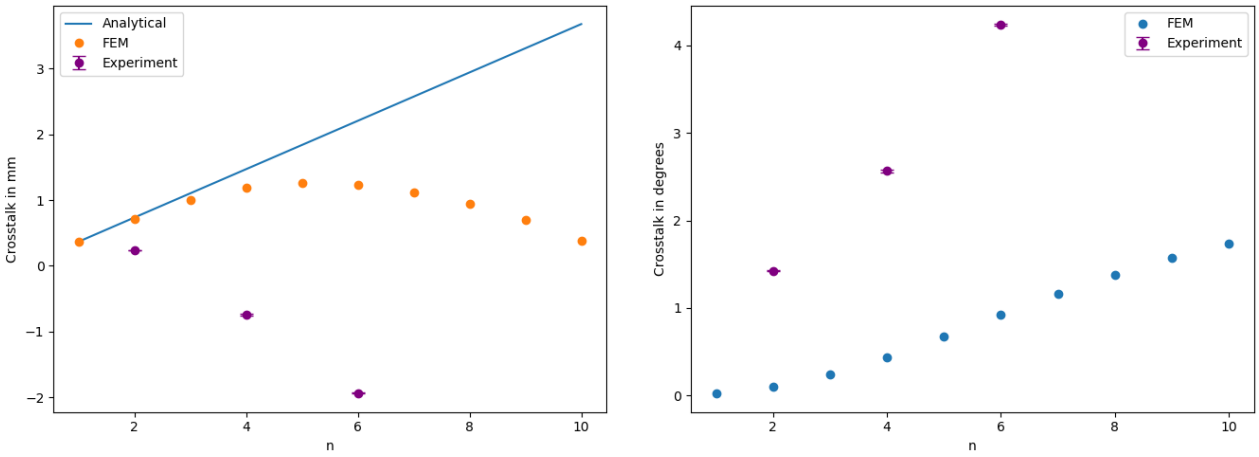

(a) Crosstalk x to y translation

(b) Crosstalk x to in plane rotation

Figure 29: Crosstalk results series tessellation

3.1.4 Series with scaling

Series with scaling maintains constant stiffness by increasing flexure thickness. Figure 30a shows the decrease in RoM per unit cell, as the yield stress is reached at decreasing displacement. Multiplied by the number of serial unit cells, the overall RoM is still increased, as shown in Figure 30b.

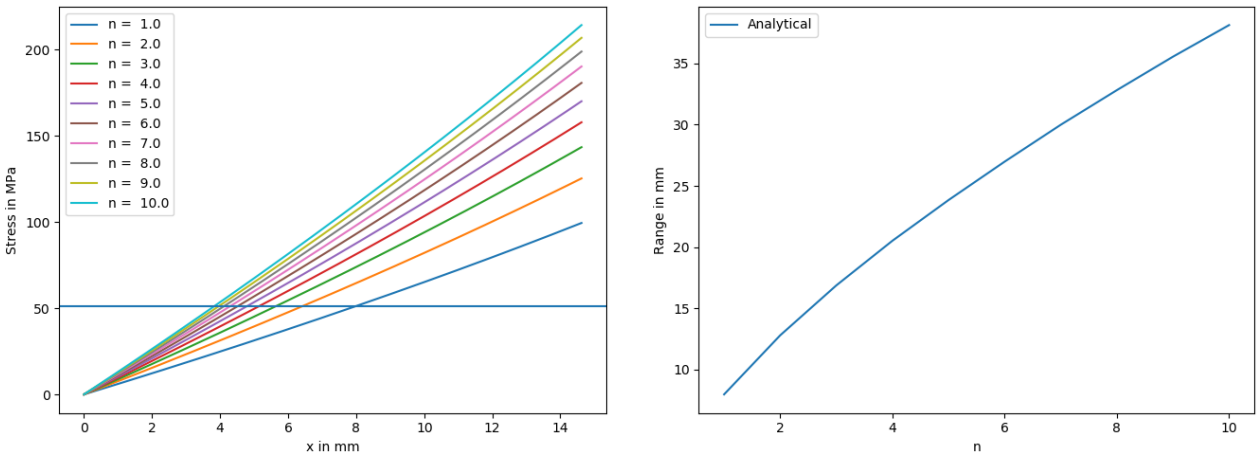

(a) Flexure stress versus x displacement series scaling.

(b) RoM series scaling

Figure 30: Stress plotted versus displacement and RoM for series scaling. (a) shows the decrease of unit cell displacement by increasing the flexure thickness. Therefore the RoM no longer increases linearly as series tessellation but at a lowering rate (b)

The analytical DoF stiffness remains constant, while the stiffness of the unit cells increases. In Figure 31a the unit cell stiffness begins at a lower value compared to the overall structure, caused by the three parallel unit cells in each row. Notably, for $m = 3$, the unit cell and overall structure intersect, indicating that the series and parallel effects effectively cancel each other out. The FEM results, depicted in Figure 31a, show a gradual decrease as n increases, which contrasts to the slight increase observed in parallel scaling. Overall the magnitude of the FEM results is lower than the analytical results, however the FEM results remain approximately constant. The experimental results are not consistent, with the first sample demonstrating higher stiff compared to the subsequent two samples, which were produced in a different batch. The samples of $m = 4$ and $m = 6$ agree well with the FEM results.

Similar to the stiffness results, the FEM results for maximum force are lower in magnitude compared to the analytical model for the overall structure. Furthermore, Figure 31b shows the decrease in force at higher unit cell numbers. This effect is consistent with the decrease in force for series arrangements. Excluding the force of the sample with higher stiffness, the subsequent samples are approximately constant in magnitude, which mirrors the behavior for the FEM results.

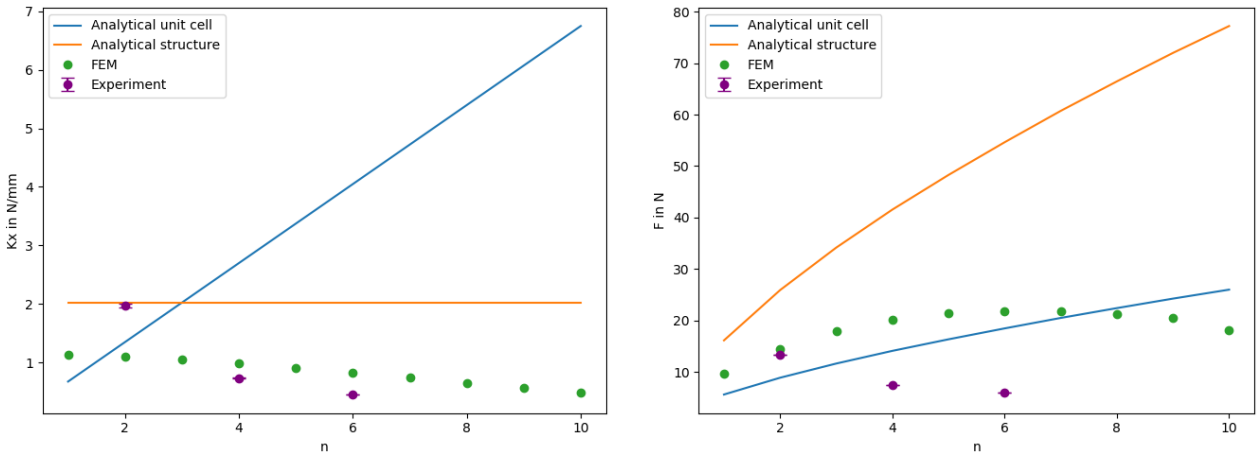

(a) Stiffness in x direction

(b) Force at maximum range

Figure 31: DoF results series with scaling t

Both constraint stiffnesses in Figure 32 increase for increasing number of unit cells. As expected, K_z decreases more at a faster rate compared to K_y. In both cases the fem results exhibit lower magnitudes, however, the experimental align closer to the FEM results.

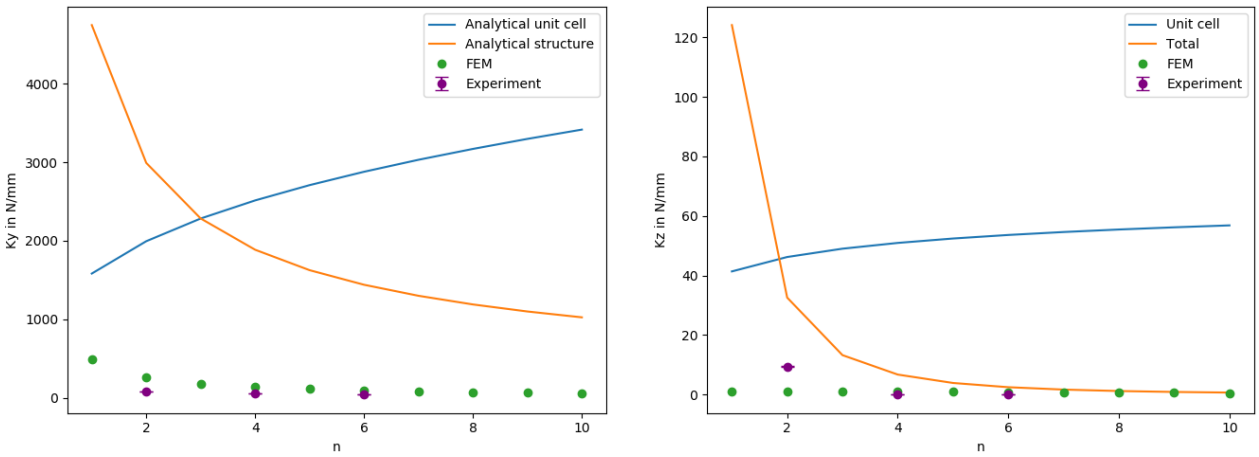

(a) Stiffness in y direction

(b) Stiffness in z direction

Figure 32: DoC results series with scaling t

Compared to the series arrangement, the RoM increases gradually less, illustrated in Figure 33a. Therefore, the translational crosstalk increases at decreasing rate. The FEM results decrease at higher number of unit cells, compared to the analytical model, which is consistent with the series arrangement. The rotation in Figure 33b is almost identical to the series arrangement. With only difference that the experimental results are closer in magnitude to the FEM results.

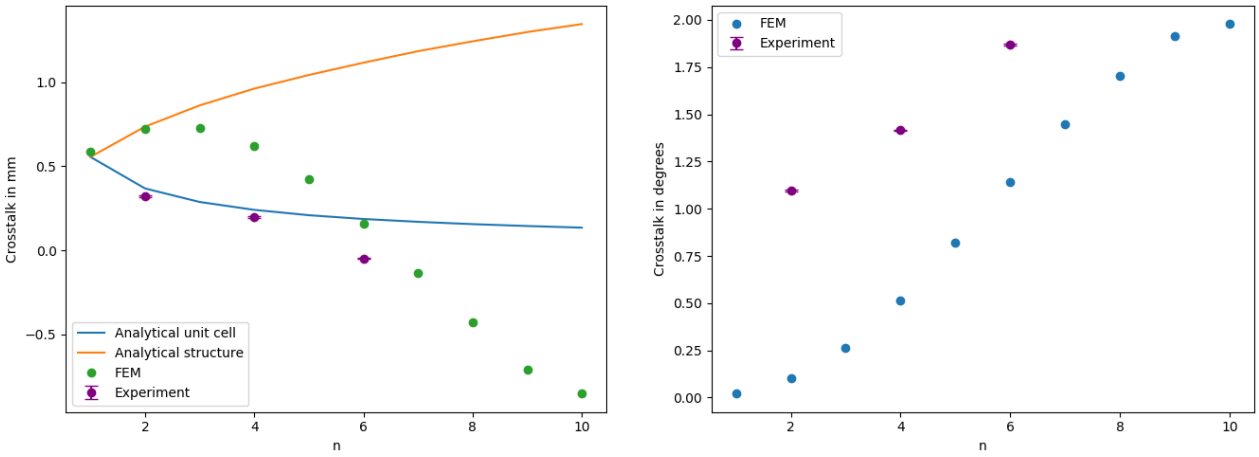

(a) Crosstalk x to y translation

(b) Crosstalk x to in plane rotation

Figure 33: Crosstalk results series with scaling t

3.2 Size of the unit cells

This section presents the effect of scaling the unit cell while the overall volume remains constant by equal number of parallel and serial unit cells.

3.2.1 Scaling all parameters

As predicted, the RoM in Figure 34 remains constant for the overall structure, while decreasing per unit cell.

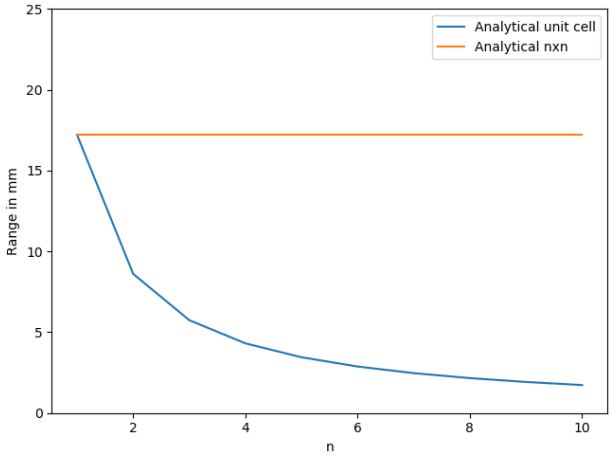

Figure 34: RoM for scaling all variables by $\frac{1}{n}$. The range per unit cell decreases with $\frac{1}{n}$, however n unit cells show a constant RoM.

Figure 35a illustrates the consistent behaviour of the unit cell and the overall structure, where the effects of series and parallel arrangement effectively cancel each other out. All datasets show close alignment, each decreasing in stiffness by $\frac{1}{n}$. The maximum force in Figure 35b similarly decreases with $\frac{1}{n}$, since the $\frac{1}{n^2}$ reduction of the unit cells is multiplied by n of the unit cells in series. The experimental results exhibit lower magnitude compared to the analytical and FEM results for the overall structure. Though, they maintain a similar decreasing trend.

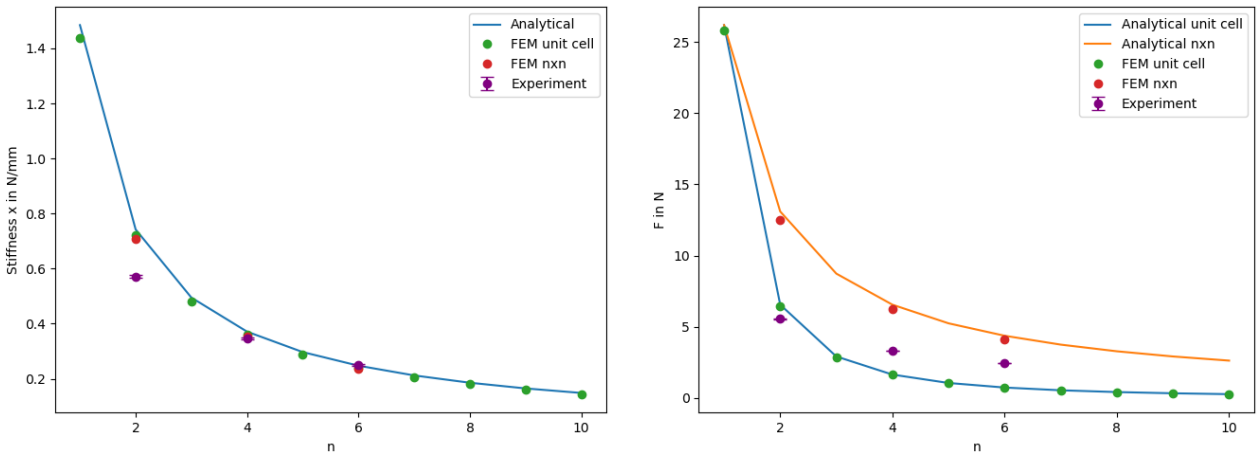

(a) Stiffness in x direction

(b) Force at maximum range

Figure 35: DoF results scaling all parameters

The stiffness in y direction shows close alignment for the FEM and experimental results, although lower in magnitude compared to the analytical results. Figure 36a shows a decreasing trend for all datasets. Figure 36b shows the out of plane stiffness of the unit cell decreasing with $\frac{1}{n}$. The overall structure decreases lower, as the serial arrangement reduces the stiffness further. Experimental results and the n by n FEM results closely align, while all FEM results are slightly lower in magnitude compared to the analytical model.

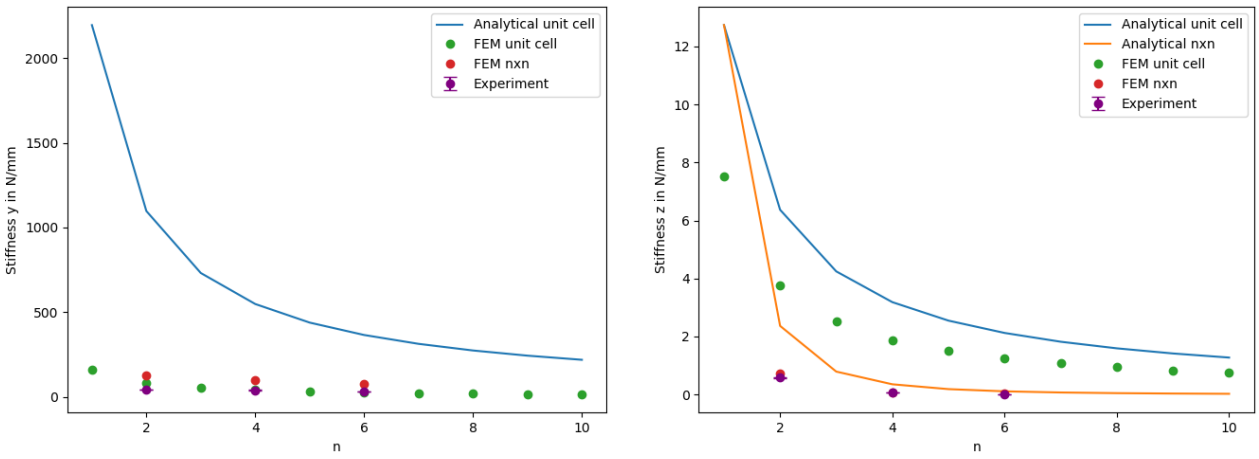

(a) Stiffness in y direction

(b) Stiffness in z direction

Figure 36: DoC results scaling all parameters

As the overall RoM remains constant, the translational crosstalk also is constant, as shown in Figure 37a. The FEM results for each unit cell align closely on the analytically predicted decreasing crosstalk; however, the overall crosstalk deviates slightly from this trend. The first two experimental results show constant magnitude, while the third result increased in magnitude. Figure 37b illustrates zero rotational crosstalk per unit cell, as the rotation is explicitly set to zero. The n by n configuration shows a constant rotation, while the experimental results reveal a decreasing trend.

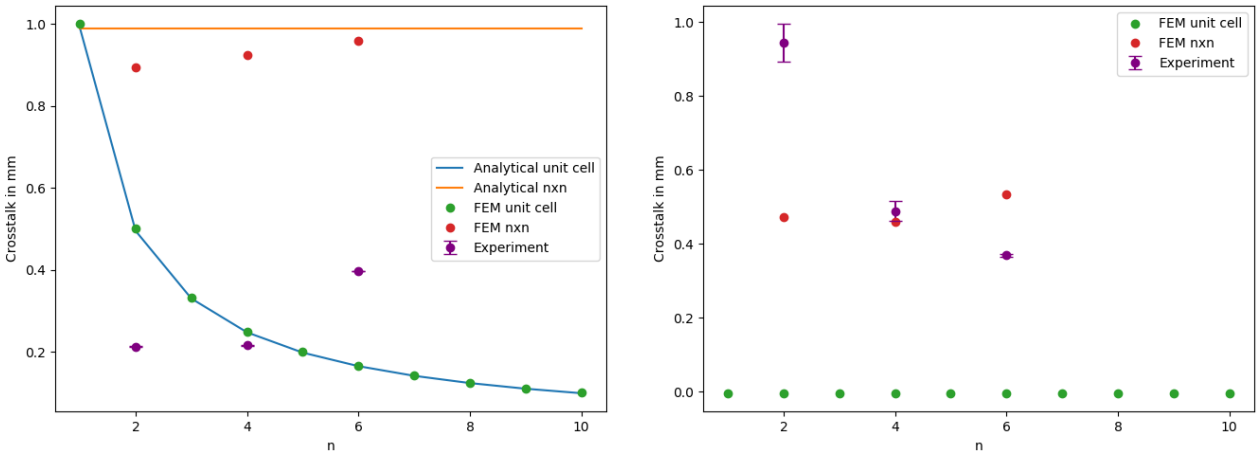

(a) Crosstalk x to y translation

(b) Crosstalk x to in plane rotation

Figure 37: Crosstalk results scaling all parameters

3.2.2 Scaling lengths and flexure thickness

Similar to scaling all parameters, the RoM in Figure 38 remains constant for the overall structure, while decreasing per unit cell.

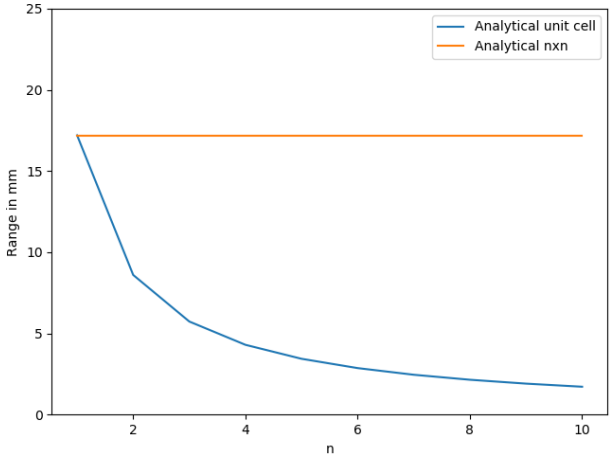

Figure 38: RoM for scaling lengths and flexure thickness by $\frac{1}{n}$. Similarly to scaling all variables, the range per unit cell decreases with $\frac{1}{n}$, however n unit cells show a constant RoM.

Figure 39a shows the DoF stiffness, which is constant for the analytical model. The FEM results show slight variation in magnitude, although insignificant. The Experimental results show a greater increase in stiffness. The force in Figure 39b shows similar behaviour as RoM, as the stiffness is approximately constant. Notable is the increasing experimental force, as the stiffness is increased. The overall magnitude of experiment is lower compared to the FEM and analytical models.

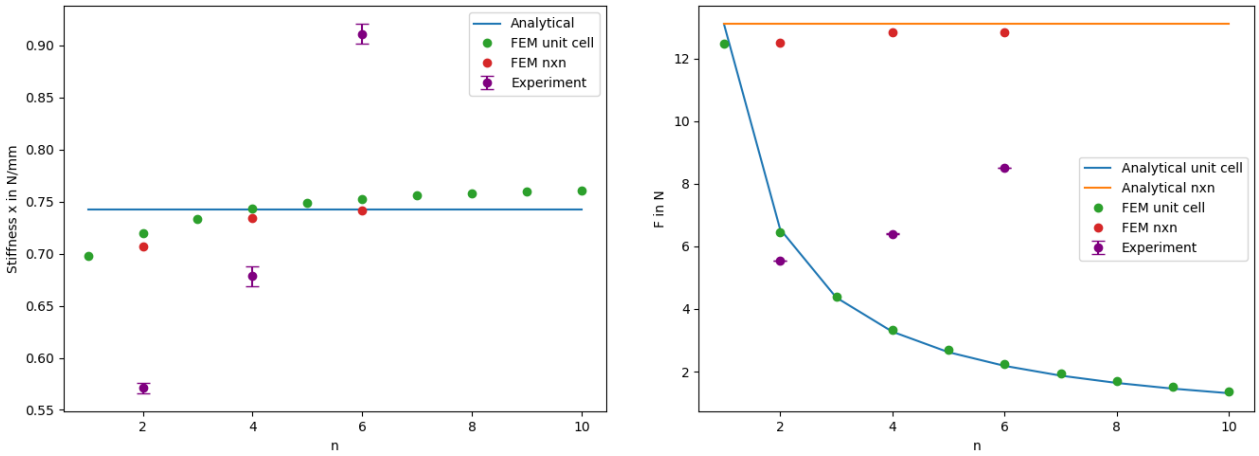

(a) Stiffness in x direction

(b) Force at maximum range

Figure 39: DoF results scaling lengths and flexure thickness

Figure 40a shows the stiffness in y direction, maintained constant for the analytical prediction. The FEM result for the unit cells is similarly maintained constant. The n by n arrangement increases in stiffness, this is similar to the greater increase of parallel units, as discussed in section 4. The experimental results are consistent with FEM n by n, although slightly lower in magnitude. The out of plane stiffness, shown in Figure 40b, gives promising results. The stiffness is approximately constant, compared to the rapid decrease of the other serial approaches. The unit cell increases in stiffness, as the out of plane thickness remains constant while the flexures decrease in length and thickness. The results for the FEM simulations vary slightly from the analytical model, although the overall trend is similar. The experimental results collide with the markers of FEM, meaning a perfect match.

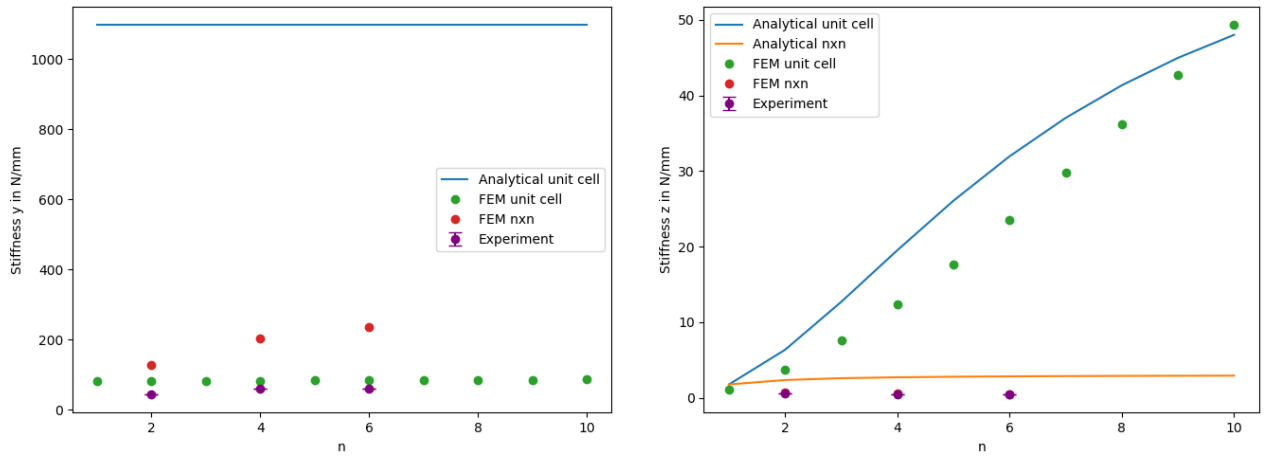

(a) Stiffness in y direction

(b) Stiffness in z direction

Figure 40: DoC results scaling lengths and flexure thickness

The analytical and FEM results for crosstalk, plotted in Figure 41a, are identical to scaling all parameters. The experimental crosstalk better illustrates the behaviour than scaling all parameters, as these results remain constant in value. Figure 41 shows that the rotational crosstalk is also identical to scaling all parameters. Similar to scaling all parameters, the experimental result also show a decreasing trend.

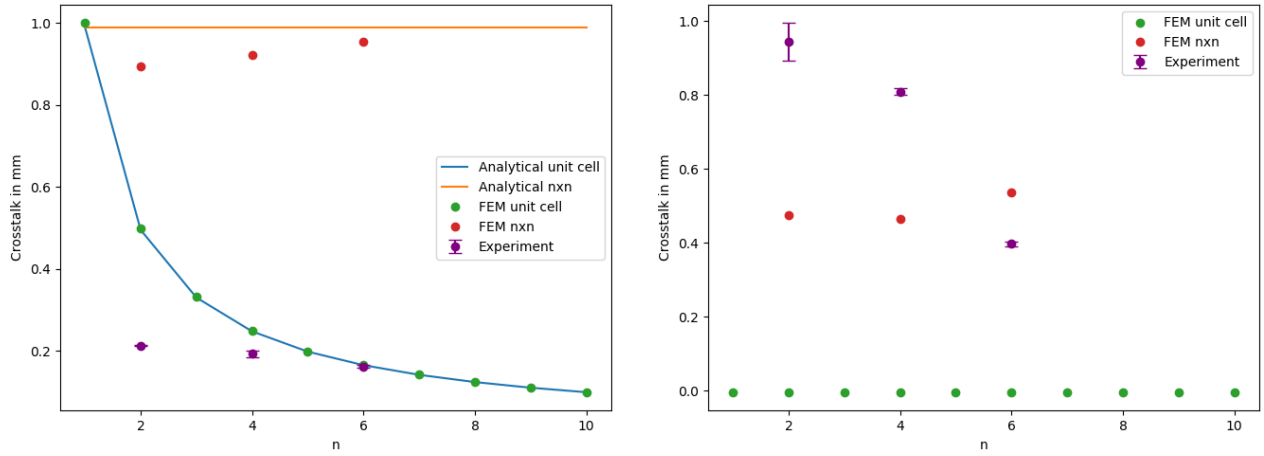

(a) Crosstalk x to y translation

(b) Crosstalk x to in plane rotation

Figure 41: Crosstalk results scaling lengths and flexure thickness

3.2.3 Scaling lengths

As seen in Figure 42 the DoF stiffness and force are predicted to increase with n^3. This leads to a higher DoF stiffness compared to the DoC stiffness, which eliminates the motion direction. Therefore this scaling method is not suitable for metamaterial motion stages.

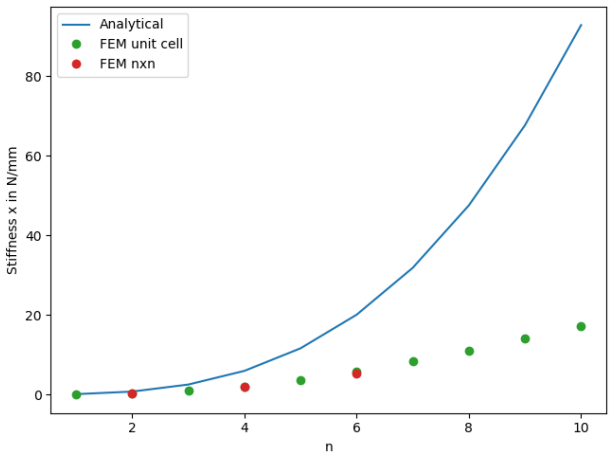

(a) Stiffness in x direction

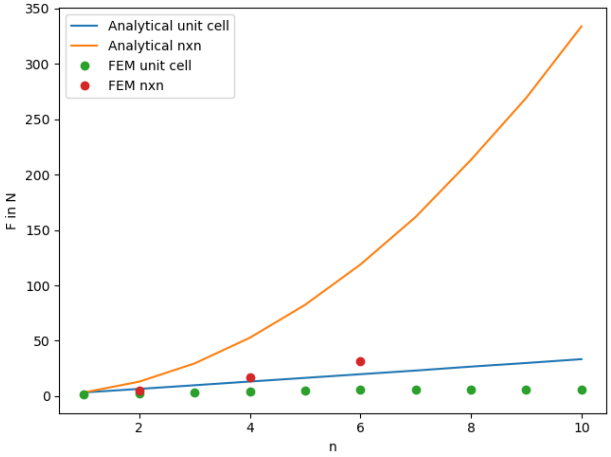

(b) Force at maximum range

Figure 42: DoF results scaling lengths

4 Discussion

The DoF stiffness showed a linear increase for parallel unit cells and a decrease of $\frac{1}{n}$ for series unit cells. The results are consistent with the assumption of the effects canceling each other out, on which the scaling analysis is based. Both series and parallel unit cells allow tuning the flexure thickness to maintain constant DoF stiffness. Scaling the unit cell behaves different depending in included the parameters. Scaling all parameters decreases the stiffness by $\frac{1}{n}$, in line with usual scaling laws. To fill a constant volume, the out of plane thickness is remained constant, resulting in constant DoF stiffness. Lastly, only scaling the in plane length dimensions, resulted in unusable high stiffness.

In plane constraint K_y showed similar behaviour to the DoF, except for tuning the flexure thickness. Out of plane stiffness K_z shows a rapid reduction in stiffness for serial unit cells. The reduction is explained by the change in boundary conditions, increasing the internal moment along the unit cells, combined with the series sum. Scaling all parameters showed similar out of plane behaviour to regular series arrangement. However, scaling lengths and flexure thickness showed approximately constant out of plane stiffness, while the unit cell increases its stiffness from increasing relative out of plane thickness. This effect can compensate the decrease in out of plane stiffness, for instance in MEMS applications where the substrate thickness is constant.

The RoM is constant for parallel unit cells and increases linearly with the number of serial unit cells. Depending on the design volume, parallel with scaling flexure thickness allows for greater RoM in a trade-off between stiffness and RoM. Scaling down the unit cells does not affect RoM. The translational crosstalk is closely related to the RoM, showing similar trends in each variation.

Most analytical results are obtained using the parallel and serial nature of unit cells, similar to compression or extension springs. Although the case study of Roberts mechanism is used to generate the graphs, similar behaviour is expected for other unit cells. Tuning the unit cell stiffness for higher RoM of parallel scaling could be used for any stress limited design. However, the constraint stiffnesses must be analysed to ensure sufficient magnitudes. Next to the type of unit cells, the results can be extrapolated for general m x n tessellations. The parallel results is derived from multiplication by the number of parallel unit cells or not changing the behaviour. This allows the series results to simply be multiplied by the parallel results, showing stiffness behaviour similar to the example in Figure 43.

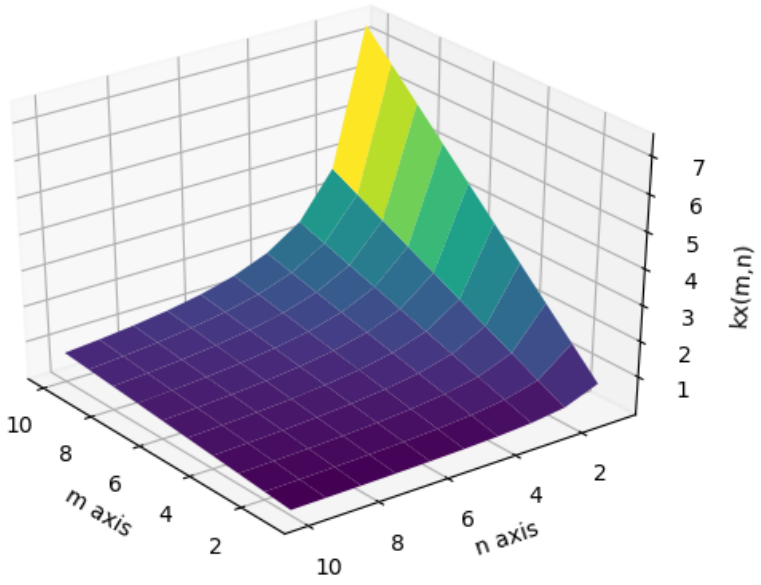

Figure 43: Example of m x n tessellation, showing the DoF stiffness as function of parallel unit cells m and series unit cells n. The analytical model plotted is $\frac{K_x m}{n}$.

Generally the analytical model, FEM simulations and experiment show similar behaviour, although there are some exceptions.

The analytical models for constraint stiffness are derived using beam equations. The in plane constraint K_y shows a different behaviour in FEM simulations compared to the analytical model, as touched upon in subsubsection 2.2.3. The buckling deformation has a lower stiffness, and therefore the magnitudes of FEM and experiment are lower than the analytical model. The out of plane stiffness K_z showed similar magnitude for

the FEM simulations and analytical model with initial dimensions, however the results deviate significantly for the adjusted dimensions. The results still allow for observing the relative behaviour changes, as the absolute values only scale the results.

For the experimental results the boundary conditions are not optimal, having limited stiffness of the output link. This measurement limit to increasing mechanism stiffness is clearly visible in the results for K_z in Figure 20bb and Figure 24b. This effect shows the importance of boundary conditions between the different models. The analytical model and simulations assume infinite stiffness of the output link, which is not well captured for the PETG samples. Increasing the thickness of the output link decreases the effect, which is not feasible as high ratios are required. For a better analysis metals could greatly increase the stiffness, also increasing the cost. As the samples were already produced, an intermediate solution was used. The aluminium H-profile, with dimensions stated in subsubsection 6.4.3, sufficiently improved the results to show the increase in stiffness.

Next to the modelling and experimental errors, there are also discrepancies for the fundamental behaviour. The parallel unit cells increase K_y at higher rate than analytically predicted. The inner vertical frames components are loaded symmetrically during compression, eliminating the bending deformation as seen in Figure 44. Eliminating the dominant bending deformation increases the stiffness as m increases, as the ratio between bending and straight frame components decreases. More specifically, two unit cells have two bending frame elements and one straight frame element, while the example of six unit cells has ratio two over five.

The rotation of the output link is not modelled, which results in great deviation for the serial results at maximum displacement. The reaction force decreases, as the deformation has an additional component. The DoF motion as calculated and the rotation of the intermediate frames multiplied by the distance to the output link. Next to the decrease in force, this also changes the results for translational crosstalk. The rotation of intermediate frames causes crosstalk that is opposite to the expansion of the unit cells.//

The results clearly outline change in behaviour from the different parallel, series and scaling variations. The project failed to identify great benefits from scaling the unit cells. The decision for metamaterial motion stages must therefore be based on different properties than the guiding structure alone. The results do however specify tools for analysis and reasoning for which variation is required. The fundamental behaviour for in plane metamaterial behaviour opens up multiple research directions. Knowledge on the mechanical guiding structure enables integrating actuation and sensing, for which the ideal distribution could be explored. The in plane, 1 DoF motion stage can be used as a building block for more complex configurations. subsection 6.6 shows different in plane and 3D configurations, allowing 2 DoF motion, greatly decreasing the crosstalk or solving the decrease in out of plane stiffness. Lastly, the knowledge can be applied to dimensioning metamaterial motion systems, bringing for instance multistability or tunable stiffness to the field of motion stages.

Figure 44: Amplified deformation in the y direction, showing the large deformations at the outer frames

5 Conclusion

This paper illustrates the behaviour change from a single compliant unit cell to a metamaterial motion system. The analysed motion system properties include linear stiffness, RoM (coupled to flexure stress) and crosstalk. The behaviour is split into two components, the number of unit cells in parallel or series arrangements and the size of the unit cells. To obtain the analysed unit cell, a novel concept of ideal shear cell is introduced. The ideal shear cell is an abstract model for motion system application, specifying the desired crosstalk and stiffness behaviour. Roberts mechanism is chosen to approximate this model, allowing embodiment of the abstract tessellation and scaling concepts.

Following the modelling process of the unit cell, analytical predictions were derived using similar analysis to compression/extension springs and scaling laws. FEM simulations and experimental results validated these predictions, demonstrating consistent behavior patterns across the three models, with notable differences discussed in section 4. In general, parallel unit cells increase the stiffness, while series unit cells decrease stiffness. Both RoM and crosstalk increase with series configurations and decrease with parallel configurations. Adjustments to flexure thickness introduce a trade-off between RoM and stiffness. Different scaling approaches, including uniform scaling and maintaining constant out of plane thickness, show constant RoM and crosstalk. The scaling results did however change in stiffness behaviour, with uniform scaling decreasing in stiffness while stiffness remains constant for constant out of plane thickness.

The study found that metamaterial tessellation, compared to traditional compliant mechanisms, does not inherently provide clear performance advantages. However, there are distinct motivations for choosing a metamaterial approach, such as the potential for internal actuation and sensing, compatibility with complex 2D or 3D tessellations and unique properties like multistability or tunable stiffness. This research provides foundational insights into the design, scaling, and performance of metamaterial motion systems, offering valuable guidelines for future development in this field.

6 Appendix

6.1 Extensive derivations

Put the formulas here that are too long for the report

Vector loop equations: Vector loop 1 can be solved by rewriting for θ_3 and using Freudenstein's equation and the half angle formula for θ_4. This leads to the following result:

Vector loop 2 can be solved by setting θ_5 to $\theta_3 + 90°$, as both r_3 and r_5 form the coupler link. This results in two unknowns for r_6, namely L_6 and θ_6. θ_6 can be solved by dividing the imaginary part by the real part of vector loop 2 and L_6 can be solved by rewriting the real component and substituting θ_6. The resulting equations are:

Force calculation[17]:

$$F\delta x = \sum_i K_i \phi_i \delta\phi_i$$

Where K_i are the rotational stiffnesses of the PRBM, following the flexure types, and ϕ_i are the relative angles between the links. For the leaf springs $K_\theta = 2.65$ and $\gamma = 0.8517$. $K_{leaf} = 2\gamma K_\Theta EI/L$ [17] and $K_{cartwheel} = 8EI/L$ [28][27]

$$\phi_1 = \theta_2 - \theta_{20}$$
$$\phi_2 = (\theta_2 - \theta_{20}) - (\theta_3 - \theta_{30})$$
$$\phi_3 = (\theta_3 - \theta_{30}) - (\theta_4 - \theta_{40})$$
$$\phi_4 = \theta_4 - \theta_{40}$$
$$\phi_5 = \theta_5 - \theta_{50} = (\theta_3 + 90°) - (\theta_{30} + 90°)$$

$$\delta\phi_1 = \delta\theta_2$$
$$\delta\phi_2 = \delta\theta_2 - \delta\theta_3$$
$$\delta\phi_3 = \delta\theta_3 - \delta\theta_4$$
$$\delta\phi_4 = \delta\theta_4$$
$$\delta\phi_5 = \delta\theta_5 = \delta\theta_3$$

To obtain δx, the small angle approximation for x is used. Here the horizontal components of each link is calculated with geometry and summed. The partial derivative to the angle is multiplied by the virtual displacement of the angle, translating the angles θ_2 and θ_3 to the respective components in δx.

$$x = x_{L2} + x_{L3} + x_{L5} = L_2 cos(\theta_2) + \frac{L_3}{2} cos(\theta_3) + L_5 sin(\theta_3)$$

Applying the general formula for virtual displacements, $\delta x = \sum_i \frac{dx}{d\theta_i}\delta\theta_i$, results in the following δx:

$$\delta x = -L_2 sin(\theta_2)\delta\theta_2 + \left(-\frac{L_3}{2} sin(\theta_3) + L_5 cos(\theta_3)\right)\delta\theta_3$$

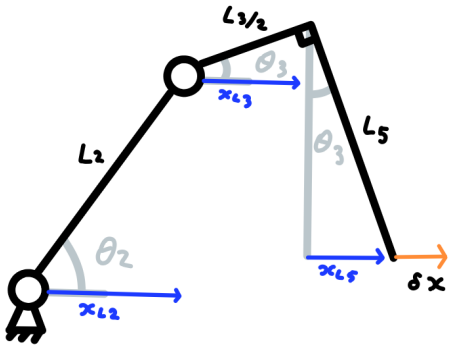

Figure 45: Sketch used to calculate the approximation of x and the convention for δx

Filling all expressions into the virtual work formula and solving for F results in:

$$F(-L_2 sin(\theta_2)\delta\theta_2 + (-\frac{L_3}{2}sin(\theta_3) + L_5 cos(\theta_3))\delta\theta_3) = K_1(\theta_2 - \theta_{2,0})\delta\theta_2 + K_2((\theta_2 - \theta_{2,0}) - (\theta_3 - \theta_{3,0}))(\delta\theta_2 - \delta\theta_3) + K_3((\theta_3 - \theta_{3,0}) - (\theta_4 - \theta_{4,0}))(\delta\theta_3 - \delta\theta_4) + K_4(\theta_4 - \theta_{4,0})\delta\theta_4 + K_5(\theta_3 - \theta_{3,0})\delta\theta_3$$

$$F = \frac{(K_1\phi_1 + K_2\phi_2)\delta\theta_2 + (K_3\phi_3 + K_5\phi_3 - K_2\phi_2)\delta\theta_3 + (K_4\phi_4 - K_3\phi_3)\delta\theta_4}{-L_2 sin(\theta_2)\delta\theta_2 + (-\frac{L_3}{2}sin(\theta_3) + L_5 cos(\theta_3))\delta\theta_3}$$

$$F = \frac{A\delta\theta_2 + B\delta\theta_3 + C\delta\theta_4}{D\delta\theta_2 + E\delta\theta_3}$$

$$F = \frac{A\delta\theta_2}{D\delta\theta_2 + E\delta\theta_3} + \frac{B\delta\theta_3}{D\delta\theta_2 + E\delta\theta_3} + \frac{C\delta\theta_4}{D\delta\theta_2 + E\delta\theta_3}$$

Taking the inverse of the three fractions, the denominators can be computed.

$$F = \frac{1}{\frac{D\delta\theta_2 + E\delta\theta_3}{A\delta\theta_2}} + \frac{1}{\frac{D\delta\theta_2 + E\delta\theta_3}{B\delta\theta_3}} + \frac{1}{\frac{D\delta\theta_2 + E\delta\theta_3}{C\delta\theta_4}} = \frac{1}{div_1} + \frac{1}{div_2} + \frac{1}{div_3}$$

$$div_1 = \frac{D}{A} + \frac{E}{A}\frac{\delta\theta_3}{\delta\theta_2}, \qquad div_2 = \frac{E}{B} + \frac{D}{B}\frac{\delta\theta_2}{\delta\theta_3}, \qquad div_3 = \frac{D}{C}\frac{\delta\theta_2}{\delta\theta_4} + \frac{E}{C}\frac{\delta\theta_3}{\delta\theta_4}$$

Using Freudenstein's kinematic coefficients for a four bar mechanism[17] the divisions of $\delta\theta$ can be computed in terms of the known lengths and angles.

$$\frac{\delta\theta_3}{\delta\theta_2} = -\frac{L_2 sin(\theta_4 - \theta_2)}{L_3 sin(\theta_4 - \theta_3)}, \qquad \frac{\delta\theta_2}{\delta\theta_3} = -\frac{L_3 sin(\theta_4 - \theta_3)}{L_2 sin(\theta_4 - \theta_2)},$$

$$\frac{\delta\theta_3}{\delta\theta_4} = \frac{\delta\theta_3}{\delta\theta_2}\frac{\delta\theta_2}{\delta\theta_4} = -\frac{L_2 sin(\theta_4 - \theta_2)}{L_3 sin(\theta_4 - \theta_3)}\frac{L_4 sin(\theta_3 - \theta_4)}{L_2 sin(\theta_3 - \theta_2)}$$

With all parameters defined, the formula is combined in python to calculate the resulting force.
Stress[17]:

$$P = \frac{4K_\theta EI\theta}{L^2 cos(\theta)}$$

$$\sigma_{max} = \frac{Pac}{2I}$$

$$a = \frac{1-\gamma}{2}L_2 + \gamma L cos(\theta_2 - \theta_{2,0}) + \frac{1-\gamma}{2}l cos(\theta_3 - \theta_{3,0})$$

For Kz the deformation is split into components of bending, force and torsion. The vertical force in Figure 46 is translated to the end of the leaf spring, resulting in a moment with magnitude rF. The resulting moment is split into a moment and torsional load on the end of the leaf spring. For this the moment is $rFcos(15)$ and the torque is $rfsin(15)$. The force and moment have a direct vertical displacement *deltay* and a sway term (kwispel term) from the angle change in the coupler link $\delta\theta$.

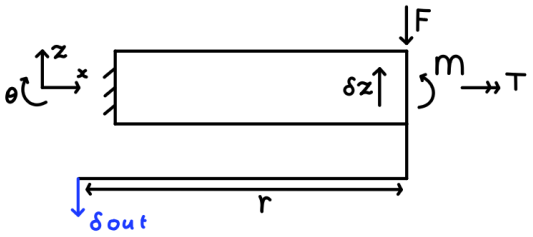

Figure 46: Sketches used to calculate K_z, showing the different load components causing deformation

For the deflection components beam equations are used for bending[32] and torsion[33].

$$F: \qquad \delta z = -\frac{FL^3}{3EI}, \qquad \delta z_\theta = r\theta_F = r\frac{FL^2}{2EI}$$

$$M: \quad \delta z = -\frac{ML^2}{2EI} = \frac{rFcos(15°)L^2}{2EI}, \quad \delta z_\theta = r\theta_m = -r\frac{ML}{EI} = -\frac{r^2Fcos(15)L^2}{2EI}$$

$$T: \quad \delta z_T = r\phi_T = -\frac{r^2Fsin(15)L}{GJ_t}$$

Dividing the force over the vertical displacement results in the stiffness, this is multiplied by two to include both leaf springs. Rewriting and taking the common terms out of brackets results in:

$$K_z = 2\frac{F}{\delta z} = \frac{2}{\frac{L}{EI}\left(\frac{L^2}{3} - \frac{rL}{2} - \frac{rLcos(15)}{2} + r^2cos(15)\right) + \frac{r^2sin(15)L}{GJ_T}}$$

The calculation for the y direction also uses beam equations. Here the load is split into an axial and bending component, as shown in Figure 47. Due to symmetry, the moment from translating the force is compensated. The angle of the load components is calculated with $\theta = 90 - 75°$.

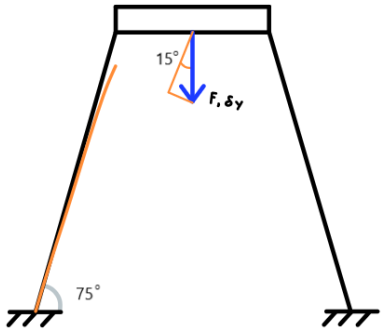

Figure 47: Sketch used to calculate K_y. The applied force or deformation are shown in blue. The separated components and the expected deformation are shown in orange.

$$K_y = K_{bending} + K_{compression}$$

$$K_y = \frac{3EI}{L^3} + \frac{EA}{L}$$

Scaling calculations

$$Stress: \quad \frac{Pac}{2I} \propto \frac{\frac{4K_\theta EI\theta}{L^2cos(\theta)}(\propto L)t/2}{2I} \propto \frac{t}{L}$$

$$K_{rotation} = 2\gamma K_\theta \frac{EI}{L} = 2\gamma K_\theta \frac{Ewt^3/12}{L}$$

From virtual work, partly filling in K and δx to calculate the scaling parameters.

$$F\delta x = K(\theta - \theta_0)\delta\theta \rightarrow F\gamma Lcos(\theta)\delta\theta = K(\theta - \theta_0)\delta\theta$$

$$F \propto \frac{2\gamma K_\theta \frac{Ewt^3/12}{L}}{\gamma Lcos(\theta)\delta} \propto \frac{wt^3}{L^2}$$

$$K_x = \frac{F}{x} \propto \frac{\frac{Ewt^3}{L^2}}{L} = \frac{wt^3}{L^3}$$

$$K_z \propto \frac{EI}{L^3} = \frac{wt^3}{L^3}$$

$$K_y \propto \frac{wt^3}{L^3} + \frac{wt}{L}$$

where the second fraction comes from crompression, and the first from bending.

6.2 Table with dimensions

The different sample dimensions are shown in Table 4. Reference is the reference dimensions[26] used for unit cell validation. The other dimensions are the unit cell for m or n = 1, except scaling using n = 2 as reference dimension. As scaling uses W = 8.25 for scaling length and flexure thickness, whereas scaling all uses W = 16.5 for the first unit cell. Except out of plane thickness W, all dimensions are illustrated in Figure 48.

Table 4: Table with dimensions for the different samples

Parameter	Reference	Series/Parallel	Series scaling	Parallel scaling	Scaling 2x2
L2, L4	36	19.8	19.8	19.8	26.64
L3	30	17.25	17.25	17.25	22.2
L5	36	19.8	19.8	19.8	26.64
L_cartwheel	-	9.6	9.6	9.6	12.58
t_leafspring	0.5	0.61	0.48	0.76	0.81
t_cartwheel	-	0.49	0.39	0.62	0.66
t_base/t_output	-	5.5	5.5	5.5	5.92
t_side	-	4.4	4.4	4.4	5.92
W	10	8.25	8.25	8.25	8.25

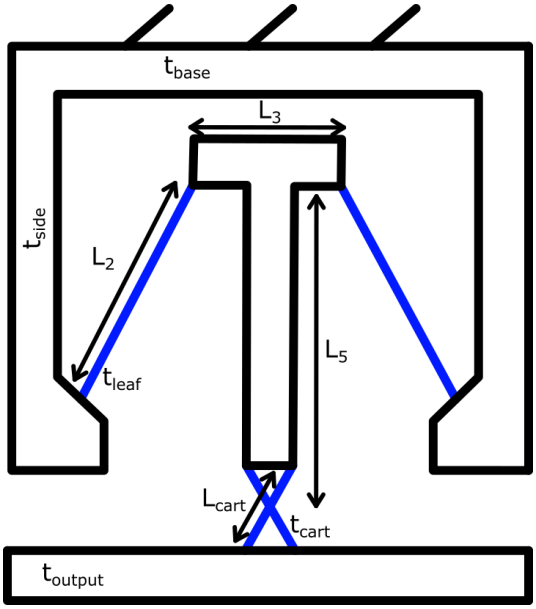

Figure 48: Convention for variables in Table 4

6.3 Simulations

6.3.1 Boundary conditions

During the project, different boundary conditions were explored. This section covers some of the behaviours resulting form the applied displacement.

Initial simulation was carried out using face actuation, along the whole output link. Total deformation does not result in the specified displacement, as the result also contains the crosstalk. Using this result causes an error in the stiffness calculation. This is avoided by probing the displacement at the output surface. Unfortunately,

Ansys does not allow for obtaining all three deformations using one feature. Therefore three different probes are applied on the output face, one for each direction. This solved the discrepancy between applied and measured displacements. One downside of this is the averaging effects over the large output surface. Internally Ansys determines how far the surface moved in the desired direction, while the output link is rotated by crosstalk. Therefore the displacement is not equal for each point of the output link, possibly resulting in small differences.

To solve the large surface effects and potential experimental actuation, a small cylindrical hole is added to the middle of the output link. This features is used to apply the deformation and probe the output displacement in three directions. This however introduces additional problems, with the output link not being infinitely stiff. This effect for the y direction is shown in Figure 49. The stiffness of the output link limits the measured stiffness, prohibiting an increase in stiffness after a limited number of parallel unit cells. A similar effect is observed for K_z. The DoF motion also requires the increased stiffness from actuating the whole surface, where moment loads of the cartwheels cause a wave pattern on the link. To overcome these problems, the full output link is displaced. This is consistent with the analytical model, where the output and base frame are assumed to be infinitely stiff.

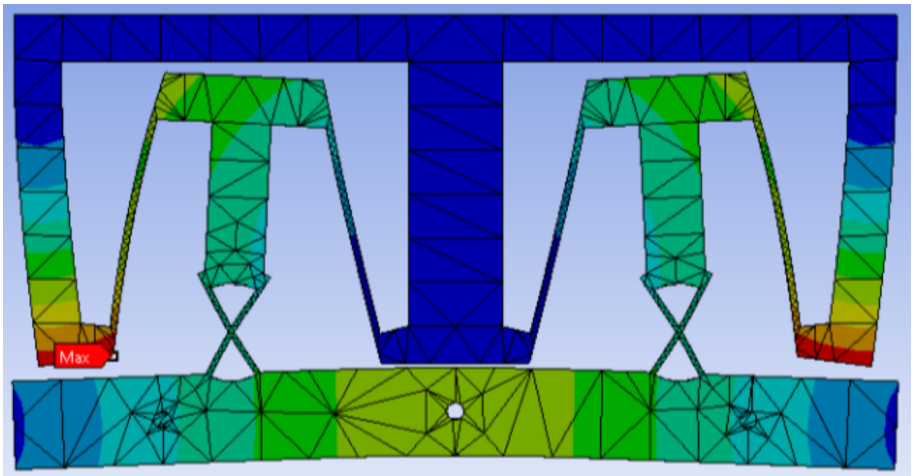

Figure 49: Displacement on the actuation center, causing deformation in the mechanism as well as the output link.

Another internal behaviour from Ansys is the angle of rotation using different methods. Applying a deformation to the actuation center resulted in a different magnitude compared to actuating the whole surface. The feature of remote displacement is investigated to explicitly set the rotation to free, this resulted in a third value for rotation. For consistency the deformation is used, still providing insights into relative changes between the samples.

If stress is accurately simulated the RoM can be verified by FEM. The stress at maximum displacement is not exactly at the yield stress, which follows from the insufficient number of elements in thickness direction. Before the extensive convergence study, the displacement was iterated to obtain the desired stress. It quickly became clear that this is not feasible for simulations as the repeated simulations take a long time and the stress is not accurate enough.

6.3.2 Convergence study

Original convergence study, no extra elements in thickness. Tried to get more elements in thickness direction but unreliable for changing geometries with the mesh constraint. Need multibody simulation to have the edge divisible (ref to multibody convergence).

Single body convergence study using the reference scale, with adjusted thickness for the material PETG. All settings are consistent with the explained FEM setup in subsection 2.4. The surfaces of the flexures are selected and different element sizes are applied. Figure 50a shows the force converging for decreasing element size. The stress does however not converge, as illustrated in Figure 50b.

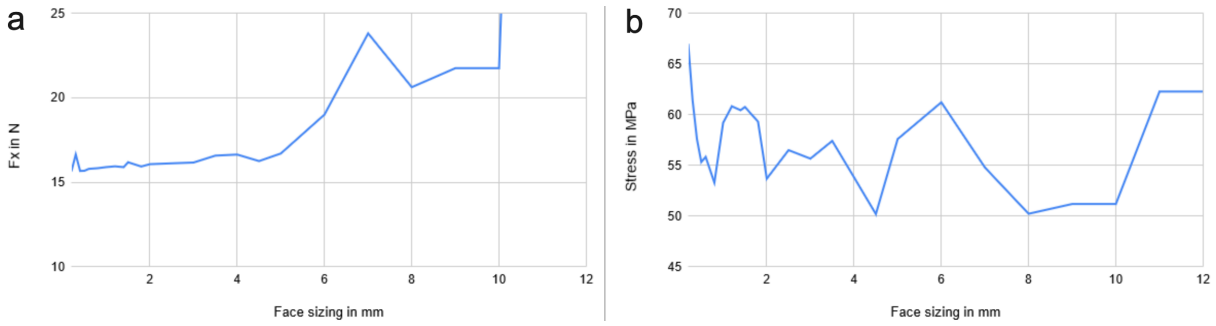

Figure 50: Convergence study (a) force and (b) stress vs the element size

Next to the convergence study, adaptive convergence was tested. Adaptive convergence allows mesh refinement based on the initial result, adding more elements based on the change in stress profile. Five refinement loops are specified, resulting in increasing stress up to about 70 MPa. This greatly overestimates the flexure stress due to the stress concentration between the flexure and coupler body. Having stress concentrations and very fine mesh can reach singularity[34]. Therefore, this method is not explored further.

6.3.3 Multibody for convergence

To investigate if the mesh of the flexures changes by adding elements in the thickness direction, a multibody part is inserted into Ansys Workbench. Having separate bodies for the flexures and rigid bodies allows better control over the mesh refinement. The flexures are rectangular boxes, resulting in rectangular mesh, where each edge can be divided into increasing number of elements. For presented analysis the in plane sizing of 1.5 mm is used, as found in subsubsection 6.3.2. Figure 51 shows the stiffness and force for the different subdivisions of the thickness direction, which does not influence the results. However, the stress result becomes more accurate by adding elements in the thickness direction. Figure 52 shows a big decrease for the first subdivision, after which a gradual decrease to the analytical result of 51 MPa is reached.

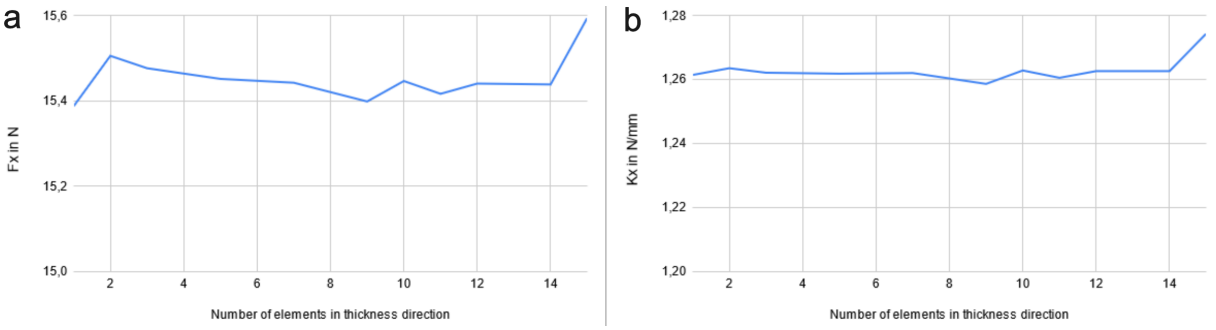

Figure 51: Convergence study multibody model (a) stiffness and (b) maximum force vs the number of thickness elements

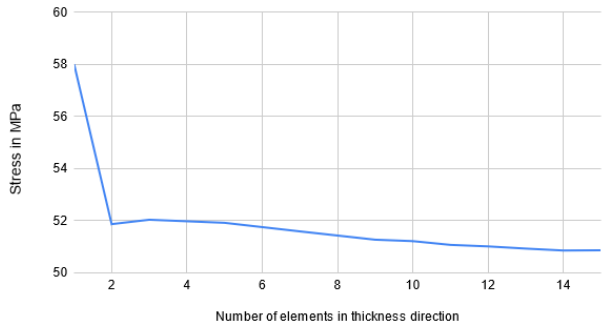

Figure 52: Convergence study stress vs thickness elements

Table 5 shows the results for different bond types in the multibody model. As observed, not all results are equal. In particular the stress varies greatly, with the force and stiffness also differing about 5%. Next to this,

Table 5: DoF results for various bond types compared to the analytical results

	Fx	Kx	Stress
standard bonds	62,4	5,12	59
MPCT1	65,45	5,406	55,9
MPCT2	65,092	5,376	53,18
MPCT10	64,809	5,3529	62,5
SharedTopT1	63,571	5,2703	59
SharedTopT2	63,27	5,2458	53,445
SingleBody	64,637	5,356	52,3
Analytical	64,312	5,4004	51

the higher number of elements in the thickness direction result in longer simulation time. Therefore, using this method was not deemed worth the additional effort.

6.3.4 Beam elements

Currently for large number of unit cells, the amount of nodes and elements is too large for simulation. Therefore it is investigated if beam elements could reduce node and element count. The multibody model is loaded into SpaceClaim, where the geometry is converted into a 1D line with a cross section. Having all flexures selected, SpaceClaim can generate the coupled cross section with function extract beams. Figure 53 shows both the multibody part and the beam model. Similar to specifying the element size on a surface, the lines are refined to 0.5 mm elements. Meshing the model results in two element types, Solid186 for the 3D bodies and Beam188 for the 1D beams. The simulation result shows that the bond contact must be refined, as the edges of the beams are not propperly connected. Comparing the number of elements shows that this feature allows larger tessellations to be simulated. The unit cell with full geometry consists of 15905 nodes and 8238 elements, where the beam model only has 4988 nodes and 898 elements.

For the current analysis it is chosen not to use this feature. The bond between the beam elements and the geometry needs further investigation and the extra operations within SpaceClaim make it less suited for constantly changing geometry. Although the feature is not used in this analysis, it showed great potential for simulating more complex tessellations in later studies.

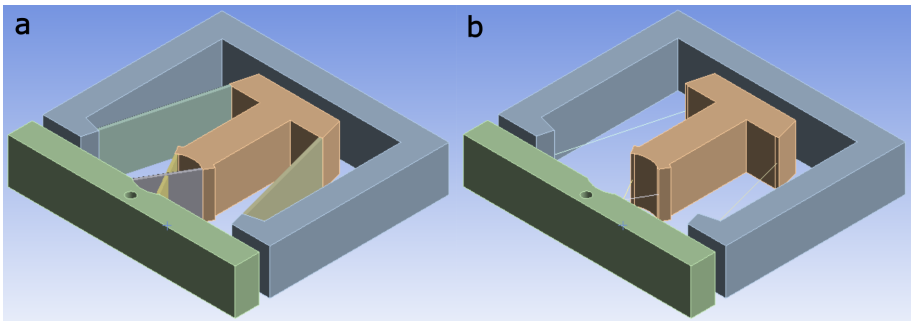

Figure 53: (a) Multibody model used for generating the beam model. (b) Beam model, replacing the flexures with 1D beam elements.

6.3.5 Yield simulation

For experimentally determining the RoM, it is investigated if yield behaviour could show in the actuation force. If the stress can be measured by yield stress, no extra sensors are required to measure strain. To learn and validate this theory, a simple tensile specimen is used[35]. A bilinear material model is used, where the stress remains constant for strains above the yielding point. Compared to the other simulations, the stress strain behaviour is path dependent. To accurately depict the yielding behaviour, the simulation substeps must be increased. For the simulation one side of the specimen is fixed, while the other side is displaced in tension. The plastic strain is shown in Figure 54a, verifying the plastic deformation. The reaction force per simulation time is plotted in Figure 54b. The force reduces after the plastic deformation is reached, caused by necking. The initial simulation showed promising results, where the plastic deformation can be simulated and detected using the actuation force.

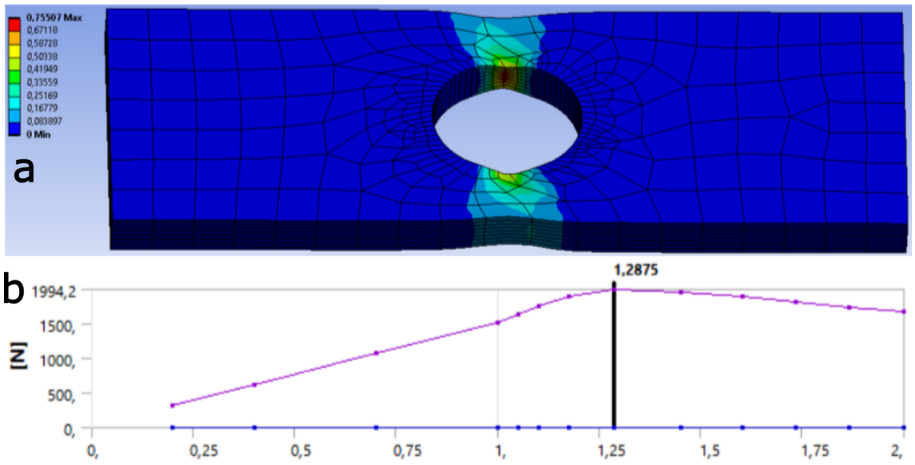

Figure 54: Yield behaviour following a tutorial [35], showing plastic strain (a) and decreasing actuation force (b)

For the unit cell of Roberts mechanism, a similar simulation is conducted. To measure the yielding behaviour, the thickness is divided into 8 elements [36]. The simulation is divided into 3 steps. In the first step the model is displaced to just under the expected yielding, after which the model is displaced futher. The second step is divided into 100 substeps to capture the yielding behaviour. Lastly the displacement is set to zero, where the plastic deformation is observed. For material properties, a bilinear model is used. The stress is constant after reaching 51 MPa for PETG. The plastic strain is shown in Figure 55a, which verifies that the material exceeds the yield stress. The yielding occurs at the stress concentration between the leaf spring and the coupler link. Figure 55b illustrates the actuation force, showing the three simulation steps. It is observed that the second, more accurate, simulation step has linear behaviour. The yielding does not significantly decrease the actuation force, therefore the RoM cannot be measured this way. To verify the yielding behaviour, the stress strain curve is shown in Figure 55c. The stress increases to the yield stress, after which the stress stays constant. Unloading shows an offset, caused by plastic deformation.

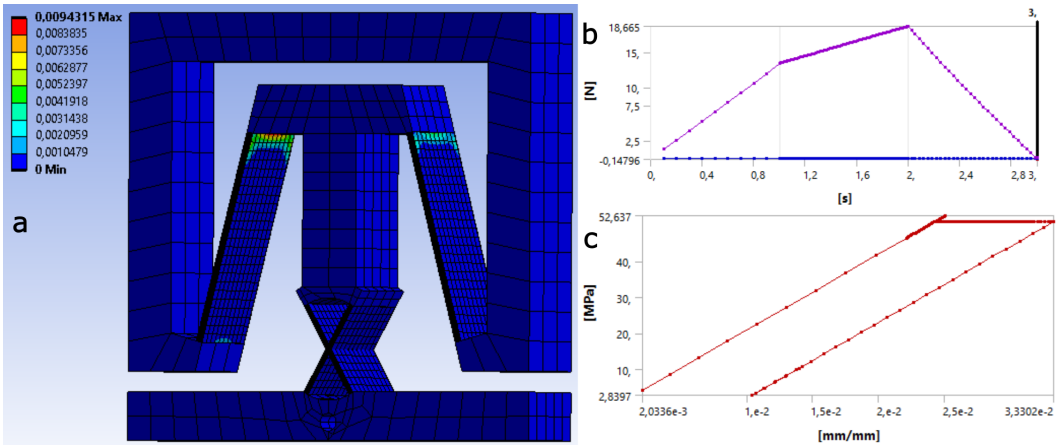

Figure 55: Yield behaviour of the unit cell. (a) plastic strain, (b) force vs simulation time and (c) stress train curve

6.4 Experiment

6.4.1 Sample fabrication

Printer and printer settings: The samples are printed on a BambuLab X1C, using a textured PEI build plate. The material is Extrudr PETG[29], which is dried before printing the samples at $55°C$ for approximately 6 hours. The spool of PETG is then stored in the all material system of BambuLab, which functions as a dry box.

25% gyroid infill for isotropic infill behaviour, 3 walls for the 0.4 mm nozzle and 4 walls for the 0.2 mm nozzle. This results in 1.2 and 0.8 mm shells, which are not comparable. Some of the results indeed showed

a lower stiffness for the 0.2 mm nozzle compared to the 0.4 mm nozzle. This was an oversight during the slicing operation. The samples for parallel, series and series scaling are produced with the 0.4 mm nozzle and the samples for parallel scaling and scaling are produced by the 0.2 mm nozzle. The samples dimensions are adjusted form the reference scale, scaling the geometry to fit onto the build plate and to allow printing of the flexures.

Initial parallel samples showed issues with seam locations at the flexures. Having two seams on the flexure greatly decreases the thickness, acting as a hinge. Therefore the stiffness of these samples is lower in magnitude. To solve this the seam locations are adjusted. Most seams are aligned on a rigid body by selecting seam location rear. The center of the cartwheel is at the rear, requiring manual adjustment. This set of seams is forced to the output link, using paint on seam locations on the geometry. Using these two methods eliminates all seams from the flexures, thereby not influencing the results.

The samples for parallel and series stacking have slight ringing between the different layers, which is caused by a deformation of the PETG spool. During drying the spool warped, causing slight extrusion inconsistencies. The effective thickness of the flexures is increased, increasing the stiffness in x direction. After this set of samples, the issue was recognised. The material was re-spooled onto a different spool, solving the issue. For the relative behaviour this deviation is still acceptable, as each unit cell shows the same effect. However, comparing the different batches of samples can deviate slightly. Additionally the flexures are measured using digital calipers. This showed deviation along each flexure, independent of production batch. Overall the dimensions are reasonably accurate, deviations in the range of 0.05 mm.

6.4.2 Specifications setup

Force sensor, steps of 0.024 N (measured/observed). Up to 45 N. 3 equivalent force sensors used. The majority of measurements are taken with Futek LSB200 - FSH03875, a 10 lb S-Beam Load Cell

For the displacement a PI motion stage is used. The resolution depends on the speed chosen in the control software in LabVIEW. The sampling time of LabVIEW is fixed, therefore the displacement depends on the speed of the motion stage. Very high resolution results in a step size of about 0.006 mm. The resolution is chosen so the resolution in force and displacement are comparable, avoiding discrete steps where possible.

For the crosstalk measurement, the Keyence LK-H052 laser displacement sensor is coupled with the LK-G5000 series controller[37]. The measurement range is 10 mm where the resolution is ensured, at absolute distance of 50 mm. Resolution is not specified, however the repeatability is 0.025 μm. The presented result on the controller, displayed as 0.001 mm, is manually noted in excel. The resolution and display values are accurate compared to the 0.1 mm required for the project. Therefore, the exact resolution is not relevant. The sensor is mounted to a slider, that can be clamped in place. The sensor is placed at one end of the slider, taking the five measurements. Then the slider is moved to the other position to take the other five measurements. The measurements are separated to avoid contacting the sensor during the actuation run, which results in positional errors of the sensor.

For linear guide a mechanism based on Roberts mechanism is used. The mechanism is shown in Figure 56, with Roberts linkage on the left. On the right is a parallelogram, used to constrain the output body to pure translation. The mechanism uses small bearings at the joints and consists of aluminium links. The mechanism is tested without a sample attached, this resulting in force below the sensor resolution.

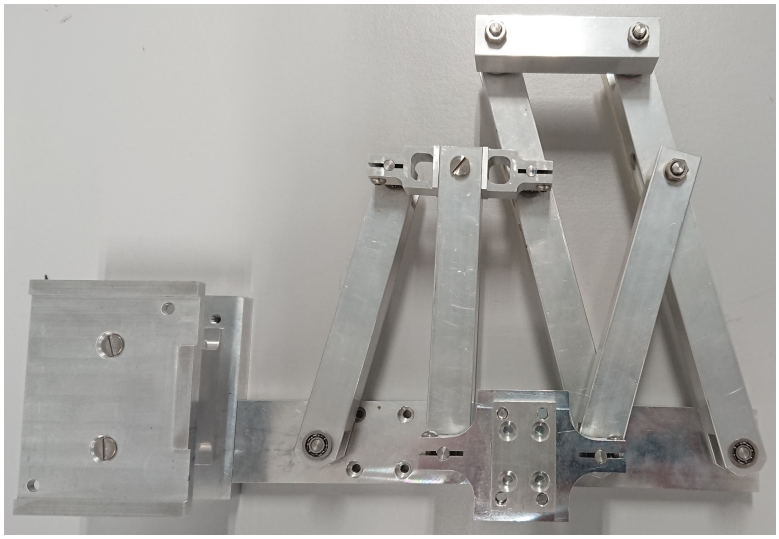

Figure 56: Linear guide used for the DoF experiments

6.4.3 Boundary conditions

Fix rotation of output but have frame rotate and move orthogonal to actuation, maybe state they should be similar? Show sketch of both setups, explain that setup 1 is more difficult and requires 3 displacement sensors instead of 2. New setup, have one low range constraint with rotation and displacement and 2 sensor positions (with 1 sensor, lack of another cable)

Initially the constraint on the base link was made using fishing wire instead of iron wire. The force of the parallel unit cells did not significantly increase, therefore the setup was investigated. Changing to two links of iron wire, did increase the parallel force. The links are made by straightening the iron wire using a cordless drill, after which the ends are bend into loops using pliers. Then the loops are connected to the sample and fixture with a bolt and some nuts, keeping the clamping force away form the iron wire.

The DoF is mounted using a quick disconnect at the guiding stage. The interface is bolted to the link, allowing tuning the rotation once. After this the sample can be mounted using a single bolt. This method seemed to work well with the force and stiffness measurements, giving consistent results. However, some samples showed creep on this connection during the crosstalk measurements. Some samples were measured multiple sessions, having slight deformation at the boundary between the plastic and aluminium. Once the issue was detected, the sample is remounted and tested again.

For the constraints the same stiffness problems were present. The initial experiment used a bolt to directly push onto the plastic sample. This resulted in a limited increase in stiffness for the parallel unit cells. Therefore an H-profile is clamped to the output frame. The profile has dimensions 9.1x12x6.5x1.3 mm. For the experiment in y direction the sample is mounted against an aluminium box profile of 15x15x1 mm. Both the aluminium profiles increases the achievable stiffness, however the effect is still present.

6.5 Dynamic study

Hao et al. [14] states that internal DoF causes dynamic problems, and therefore the intermediate bodies should be constrained. Metamaterials have many rows of unit cells, resulting in many internal DoF. It is investigated if the internal degrees of freedom from series stacking change the eigenmodes. If the internal DoF indeed pose issues, the designer should constrain the relative motion between the metamaterial rows.

To calculate resonance frequencies and mode shapes the same geometries as scaling L and t are used. The simulations are carried out in Ansys Workbench, modal module. For the simulation the material is PETG and the mesh is sized as subsubsection 6.3.2. The base link is constrained with a fixed boundary condition, as seen in subsubsection 6.3.1. Running the simulation returns the first six modes.

Table 6 shows the first eigenfrequency, belonging to the desired motion. It is observed that the resonance frequency marginally increases as the number of n by n unit cells increase. The higher order resonance modes show a bigger change in behaviour. Table 7 shows the second to sixth modes, frequency and a description of deformation. The results show that internal resonance and out of plane resonance switch places, depending on which stiffness is lowest. It is also observed that the more unit cells are added, the more internal resonance

modes occur in the DoF direction. All in all the internal resonance does not pose immediate problems for designing a metamaterial.

Table 6: First resonance frequency (DoF) for square n x n geometries

n x n	Frequency [Hz]
1 x 1	35.6
2 x 2	43.8
4 x 4	45.4
6 x 6	52.8

Table 7: Second up to the sixth resonance frequencies and mode shapes for square n x n geometries

Mode		Frequency [Hz]	Mode shape
1 x 1	2	75.4	DoF with extra rotation cartwheel
	3	169	Out of plane bending
	4	202	Out of plane rotation
	5	309	Intermediate body out of plane
	6	325	In plane translation, y direction
2 x 2	2	116	Internal resonance, DoF direction
	3	130	Out of plane bending
	4	277	Out of plane rotation
	5	385	In plane rotation
	6	495	In plane translation, y direction
4 x 4	2	116	Out of plane bending
	3	133	Internal resonance 1, DoF direction
	4	207	Internal resonance 2, DoF direction
	5	232	Out of plane rotation
	6	259	Internal resonance 3, DoF direction
6 x 6	2	113	Out of plane bending
	3	157	Internal resonance, DoF direction
	4	193	Out of plane rotation
	5	258	Internal resonance, DoF direction
	6	341	Internal resonance, DoF direction

6.6 Metamaterial sheets as a building block

Having the in plane tessellation of n by n unit cells results in sheets of metamaterial. These sheets can be used as building blocks for more complex tessellations, in or out of plane. This section covers a number of initial simulations to elaborate on this concept. A reference a sheet of 4 by 4 unit cells is used, with 36 mm leaf springs at 1.5 mm element size. The reference sheet is shown in Figure 57, showing the fixed support in blue and the actuation hole in orange. As will become clear during the section, some issues regarding out of plane stiffness can be solved by the 3D tessellation methods. Additionally, serial stacking can achieve 2 DoF motion or parallel methods for reducing crosstalk.

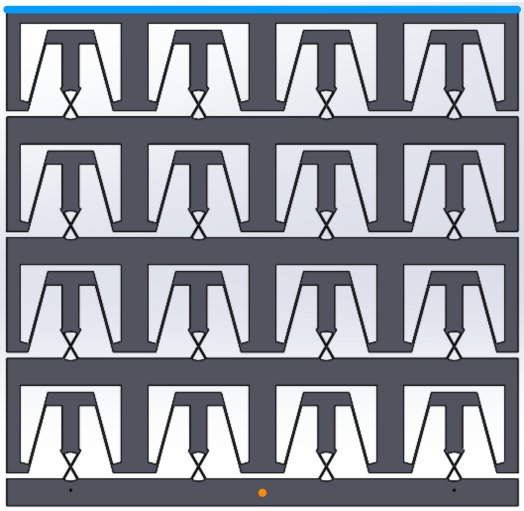

Figure 57: Geometry for 4x4 reference sheet, actuation at the center of the output link.Fixed surfaces shown in blue and actuation point shown in orange.

6.6.1 Opposing

Similar to Wan and Xu [26], the metamaterial sheets are placed in symmetric configuration. The reference paper stated a reduction in crosstalk of 60 times. The sample used for simulation and the boundary conditions are shown in Figure 58.

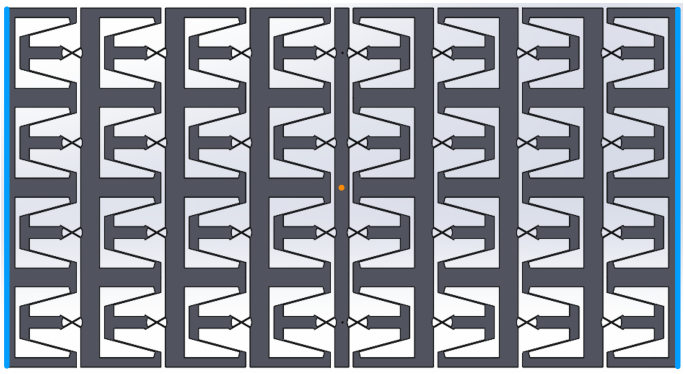

Figure 58: Geometry for opposing sheets, actuation at the center. Fixed surfaces shown in blue and actuation point shown in orange.

The simulation results are shown in Table 8. Doubling the number of parallel unit cells similarly doubles the DoF stiffness. The out of plane stiffness is increased greater than doubling, form the change in boundary conditions. The output link is no longer a free end, resulting in a moderate stiffness increase. Having both material sheets pressing into each other increases the stress and greatly reduces the crosstalk. Looking at the intermediate simulation steps, the stress is at a comparable level to the reference design at 37 mm compared to 46 mm. Calculation shows a decrease in RoM of 20% for a reduction in crosstalk of 99.97%. The simulation is still an ideal situation, so the decrease might differ in experimental validation. For reducing crosstalk this method shows great potential.

Table 8: Behaviour change opposing metamaterial sheets compared to the reference material

Sample	K_x (N/mm)	K_y (N/mm)	$K_z(N/mm)$	Stress (MPa)	Crosstalk (mm)
Reference	1.31	193	1.41	58	2.47
Opposing	2.63	258	3.73	81	6.6E-4

6.6.2 Orthogonal

Most serial arrangements showed great reduction in out of plane stiffness. To solve this issue metamaterial sheets are placed in a 3D configuration. The orthogonal sheets have symmetric constraint geometry in y and z directions. Figure 59 shows the simulated model.

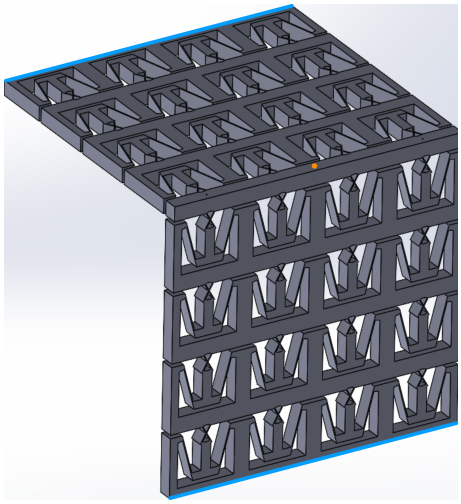

Figure 59: Geometry for orthogonal sheets, actuation at the connected output links.Fixed surfaces shown in blue and actuation point shown in orange.

The results are shown in Table 9. Similar to opposing unit cells the DoF stiffness doubles from doubling the parallel unit cells. Observed is an identical stiffness for the y and z directions, indeed solving the great reduction in out of plane stiffness. As seen the RoM and crosstalk are not significantly affected.

Table 9: Behaviour change orthogonal metamaterial sheets compared to the reference material

Sample	K_x (N/mm)	K_y (N/mm)	$K_z(N/mm)$	Stress (MPa)	Crosstalk (mm)
Reference	1.31	193	1.41	58	2.47
Orthogonal	2.63	196	196	59	2.44

6.6.3 Revolved sheets

A general revolve operation for three metamaterial sheets is simulated. The opposing and orthogonal configurations are special shapes for 2 sheets revolved 180° and 90°. The model is shown in Figure 60.

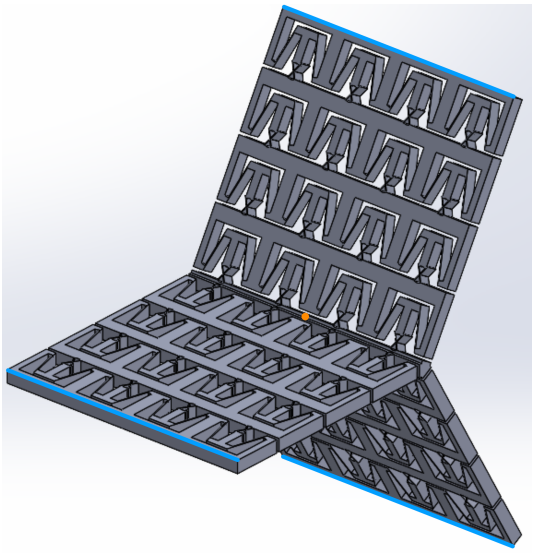

Figure 60: Geometry for revolved sheets, actuation at the center connection.Fixed surfaces shown in blue and actuation point shown in orange.

The results of Table 10 show similar behaviour to orthogonal and opposing configurations. The stiffness in y and z directions are equal. The DoF stiffness is now three times the reference stiffness as the number of parallel sheets is increased to three. Similar to the opposing configuration, the RoM is reduced while crosstalk largely cancels out.

Table 10: Behaviour change revolved metamaterial sheets compared to the reference material

Sample	K_x (N/mm)	K_y (N/mm)	$K_z(N/mm)$	Stress (MPa)	Crosstalk (mm)
Reference	1.31	193	1.41	58	2.47
Revolved	3.95	277	276	80	6.2E-4

6.6.4 Alternating

Similar to error compensation, with case study Xbob[24], the metamaterial sheets are placed in alternating configuration. It is investigated if the metamaterial sheets have the same canceling effect as changing the unit cell itself. Figure 61 shows the used configuration, with fixed surface on one side and the actuated open end on the other side.

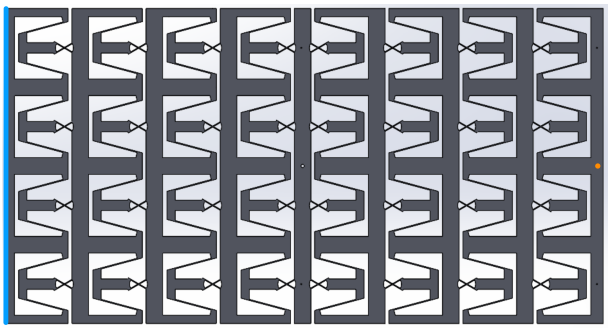

Figure 61: Geometry for alternating sheets, actuation at the far right.Fixed surfaces shown in blue and actuation point shown in orange.

As observed in Table 11, the additional serial unit cells decrease the stiffness values. The most important results is the crosstalk, not showing a decrease. The value is less than double, likely due to the additional rotation of the doubling of unit cells in series. The fact that this method doesn't work is clear in hindsight. The unit cell expands during motion, alternating the metamaterial still expands the unit cells and therefore adds to the overall crosstalk. Having a more complex out of plane configuration potentially solves this, similar to the folded flexure design.

Table 11: Behaviour change alternating metamaterial sheets compared to the reference material

Sample	K_x (N/mm)	K_y (N/mm)	$K_z(N/mm)$	Stress (MPa)	Crosstalk (mm)
Reference	1.31	193	1.41	58	2.47
Alternating	0.62	135	0.2	65	3.2

6.6.5 2 DoF in series

In plane and card house, increase crosstalk? In plane: Kx a little more stiff than ky. Kz very low but comparable to the drop in series tessellation. A serial approach for obtaining 2 DoF is simulated. The method used is in plane, however similar simulations can be carried for different out of plane configurations. The simulated geometry is shown in Figure 62.

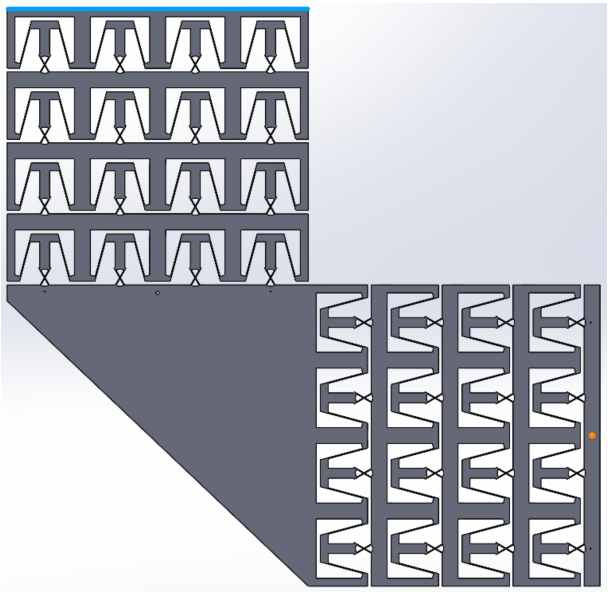

Figure 62: Geometry for 2 DoF motion, in plane series configuration. Fixed surfaces shown in blue and actuation point shown in orange.

As observed in Table 12, the x and y directions are close in stiffness. The difference comes from the loading condition, where one direction is connected to ground while the other direction is connected to an intermediate body. Similar to the difference in static behaviour, it is expected that the different loading conditions cause a difference in dynamic performance. The out of plane stiffness decreases similar to a doubling in serial unit cells, having a slightly higher magnitude.

Table 12: Behaviour change 2 DoF configuration of metamaterial sheets compared to the reference material

Sample	K_x (N/mm)	K_y (N/mm)	$K_z(N/mm)$	Stress (MPa)	Crosstalk (mm)
Reference	1.31	193	1.41	58	2.47
2 DoF	1.25	1.15	0.28	50	2.3E-2

References

[1] Zhenwei Wang et al. "Progress in Auxetic Mechanical Metamaterials: Structures, Characteristics, Manufacturing Methods, and Applications". In: *Advanced Engineering Materials* 22.10 (2020), p. 2000312. DOI: https://doi.org/10.1002/adem.202000312.

[2] Jianxing Liu and Yihui Zhang. "Soft network materials with isotropic negative Poisson's ratios over large strains". In: *Soft Matter* 14 (5 2018), pp. 693–703. DOI: http://doi.org/10.1039/C7SM02052J.

[3] Qing Li, Deqing Yang, and Xiang Mao. "Pressure-resistant cylindrical shell structures comprising graded hybrid zero Poisson's ratio metamaterials with designated band gap characteristics". In: *Marine Structures* 84 (2022), p. 103221. ISSN: 0951-8339. DOI: https://doi.org/10.1016/j.marstruc.2022.103221.

[4] A Alderson and K L Alderson. "Auxetic materials". In: *Proceedings of the Institution of Mechanical Engineers, Part G: Journal of Aerospace Engineering* 221.4 (2007), pp. 565–575. DOI: https://doi.org/10.1243/09544100JAERO185.

[5] Jochen Mueller, Jennifer A. Lewis, and Katia Bertoldi. "Architected Multimaterial Lattices with Thermally Programmable Mechanical Response". In: *Advanced Functional Materials* 32.1 (2022), p. 2105128. DOI: https://doi.org/10.1002/adfm.202105128.

[6] Claudio Findeisen et al. "Characteristics of mechanical metamaterials based on buckling elements". In: *Journal of the Mechanics and Physics of Solids* 102 (2017), pp. 151–164. ISSN: 0022-5096. DOI: https://doi.org/10.1016/j.jmps.2017.02.011.

[7] Hang Yang and Li Ma. "1D to 3D multi-stable architected materials with zero Poisson's ratio and controllable thermal expansion". In: *Materials and Design* 188 (2020), p. 108430. ISSN: 0264-1275. DOI: https://doi.org/10.1016/j.matdes.2019.108430.

[8] Bihui Zou et al. "Magneto-Thermomechanically Reprogrammable Mechanical Metamaterials". In: *Advanced Materials* 35.8 (2023), p. 2207349. DOI: https://doi.org/10.1002/adma.202207349.

[9] J. H. Burge. *Motion control: Stages*. Arizona, 2016. URL: https://wp.optics.arizona.edu/optomech/wp-content/uploads/sites/53/2016/08/23-stages-1.pdf.

[10] Chenyang Luo et al. "Design and fabrication of a three-dimensional meso-sized robotic metamaterial with actively controlled properties". In: *Mater. Horiz.* 7 (1 2020), pp. 229–235. DOI: http://doi.org/10.1039/C9MH01368G.

[11] Yong Zhang et al. "Design and characterization of multi-stable mechanical metastructures with level and tilted stable configurations". In: *Extreme Mechanics Letters* 34 (2020), p. 100593. ISSN: 2352-4316. DOI: https://doi.org/10.1016/j.eml.2019.100593.

[12] Alexandra Ion et al. "Metamaterial Mechanisms". In: *Proceedings of the 29th Annual Symposium on User Interface Software and Technology*. UIST '16. Tokyo, Japan: Association for Computing Machinery, 2016, pp. 529–539. ISBN: 9781450341899. DOI: https://doi.org/10.1145/2984511.2984540.

[13] Bennett McCarthy et al. "Design of configuration indifferent compliant building blocks". In: *Precision Engineering* 81 (2023), pp. 60–67. ISSN: 0141-6359. DOI: https://doi.org/10.1016/j.precisioneng.2023.02.002.

[14] Guangbo Hao et al. "Conceptual design of compliant translational joints for high-precision applications". In: *Frontiers of Mechanical Engineering* 9.4 (2014), pp. 331–343. ISSN: 2095-0241. DOI: https://doi.org/10.1007/s11465-014-0321-y.

[15] Lucas A. Shaw et al. "Compliant rolling-contact architected materials for shape reconfigurability". In: *Nature Communications* 9.1 (2018), p. 4594. ISSN: 2041-1723. DOI: https://doi.org/10.1038/s41467-018-07073-5.

[16] Kevin T. Riutort. *Applied Design and Implementation of Straight-Line Mechanisms*. Master's thesis. Blacksburg, Virginia, 1996. URL: https://vtechworks.lib.vt.edu/server/api/core/bitstreams/0aa0508a-4dbe-4fd4-8d27-e1c62b11bd00/content.

[17] L.L. Howell. *Compliant Mechanisms*. A Wiley-Interscience publication. Wiley, 2001. ISBN: 9780471384786.

[18] Xu Pei et al. "Design of compliant straight-line mechanisms using flexural joints". In: *Chinese Journal of Mechanical Engineering* 27.1 (2014), pp. 146–153. ISSN: 2192-8258. DOI: https://doi.org/10.3901/CJME.2014.01.146.

[19] J. Hricko. "Design of compliant micro-stage based on Peaucellier-Lipkin straight-line mechanism". In: *2014 23rd International Conference on Robotics in Alpe-Adria-Danube Region (RAAD)*. 2014, pp. 1–6. DOI: https://doi.org/10.1109/RAAD.2014.7002262.

[20] Wikipedia. *Peaucellier–Lipkin linkage — Wikipedia, The Free Encyclopedia*. http://en.wikipedia.org/w/index.php?title=Peaucellier%E2%80%93Lipkin%20linkage&oldid=1136130739. [Online; accessed 08-December-2023]. 2023.

[21] Wikipedia. *Sarrus linkage — Wikipedia, The Free Encyclopedia*. http://en.wikipedia.org/w/index.php?title=Sarrus%20linkage&oldid=1158075437. [Online; accessed 12-December-2023]. 2023.

[22] Muhammad Rehan et al. "Anchoring Mechanism for Capsule Endoscope: Mechanical Design, Fabrication and Experimental Evaluation". In: *Micromachines* 13.12 (2022). ISSN: 2072-666X. DOI: https://doi.org/10.3390/mi13122045.

[23] Hongzhe Zhao, Shusheng Bi, and Jingjun Yu. "A novel compliant linear-motion mechanism based on parasitic motion compensation". In: *Mechanism and Machine Theory* 50 (2012), pp. 15–28. ISSN: 0094-114X. DOI: https://doi.org/10.1016/j.mechmachtheory.2011.11.009.

[24] Zhao Hongzhe et al. "Design of a Family of Ultra-Precision Linear Motion Mechanisms". In: *Journal of Mechanisms and Robotics* 4.4 (2012), p. 041012. ISSN: 1942-4302. DOI: https://doi.org/10.1115/1.4007491.

[25] Nathan C. Toone et al. "Investigation of Unique Carbon Nanotube Cell Restraint Compliant Mechanisms". In: *Mechanics Based Design of Structures and Machines* 42.3 (2014), pp. 343–354. DOI: https://doi.org/10.1080/15397734.2014.908298.

[26] Sicong Wan and Qingsong Xu. "Design and analysis of a new compliant XY micropositioning stage based on Roberts mechanism". In: *Mechanism and Machine Theory* 95 (2016), pp. 125–139. ISSN: 0094-114X. DOI: https://doi.org/10.1016/j.mechmachtheory.2015.09.003.

[27] D. Farhadi Machekposhti, N. Tolou, and J. L. Herder. "A Review on Compliant Joints and Rigid-Body Constant Velocity Universal Joints Toward the Design of Compliant Homokinetic Couplings". In: *Journal of Mechanical Design* 137.3 (Mar. 2015), p. 032301. ISSN: 1050-0472. DOI: https://doi.org/10.1115/1.4029318.

[28] L. L. Howell, S. P. Magleby, and B. M. Olsen. *Handbook of compliant mechanisms*. John Wiley & Sons, 2013.

[29] 3DJake. *Extrudr PETG Oranje*. URL: https://www.3djake.nl/extrudr/petg-oranje-1.

[30] F. Mujika et al. "Determination of tensile and compressive moduli by flexural tests". In: *Polymer Testing* 25.6 (2006), pp. 766–771. DOI: https://doi.org/10.1016/j.polymertesting.2006.05.003.

[31] BME MM. *SOLID187*. URL: https://www.mm.bme.hu/~gyebro/files/ans_help_v182/ans_elem/Hlp_E_SOLID187.html.

[32] JPE - Precision Point. *Beam theory: Bending*. URL: https://www.jpe-innovations.com/precision-point/beam-theory-bending/.

[33] JPE - Precision Point. *Beam theory: Torsion*. URL: https://www.jpe-innovations.com/precision-point/beam-theory-bending/.

[34] Łukasz Skotny. *Stress singularity – an honest discussion*. 2017. URL: https://enterfea.com/stress-singularity-an-honest-discussion/.

[35] Ansys Learning. *Evaluating Stress and Yielding in Metal Plasticity Using Ansys Mechanical — Lesson 2*. Aug. 2020. URL: https://www.youtube.com/watch?v=ai-9bRyeoqA.

[36] peteroznewman. *Plastic deformation control*. URL: https://innovationspace.ansys.com/forum/forums/topic/plastic-deformation-control/.

[37] ArtisanTG. *Keyence LK-G Series Datasheet*. URL: https://www.artisantg.com/info/Keyence_LK_G5001_Datasheet2_2021915103438.pdf.